Available online at www.sciencedirect.com
SCIENCE DIRECT®
Coordination Chemistry Reviews 249 (2005) 209–228
COORDINATION CHEMISTRY REVIEWS
www.elsevier.com/locate/ccr

Review

Photoionization cross-sections: a guide to electronic structure

Jennifer C. Green [a,*], Piero Decleva [b]

[a] *Inorganic Chemistry Laboratory, Oxford University, South Parks Road, Oxford OX1 3QR, UK*
[b] *Dipartimento di Scienze Chimiche, Università di Trieste, Via L. Giorgieri 1, I-34127 Trieste, Italy*

Received 10 June 2003; accepted 6 February 2004
Available online 13 May 2004

Contents

Abstract

The article is concerned with photoelectron (PE) spectroscopy of transition metal molecules. The use of synchrotron radiation to measure the change in intensity of photoelectron bands with photon energy, and the presentation of these results in terms of photoionization cross-sections and branching ratios are described. The qualitative interpretation of PE cross-sections is outlined and illustrated with data from metallocenes and tetrahedral molecules. The successes and failures of the Gelius model are discussed. Methods of calculating ionization energies are presented and evaluated. Calculation of photoionization cross-sections is shown to provide a good account of many of the experimental features. Overall, the measurement and interpretation of PE data gives support to modern theoretical methods of describing the electronic structure of transition metal molecules.

Keywords: Variable photon energy photoelectron spectroscopy; Transition metal molecules; Photoionization cross-sections; Ionization energies; Molecular orbitals

1. Introduction

Photoelectron (PE) spectroscopy measures the binding energies of electrons in molecules [1]. Ionization, promoted by

* Corresponding author. Fax: +44-1-1865-272690.
E-mail address: jennifer.green@chem.ox.ac.uk (J.C. Green).

0010-8545/$ – see front matter © 2004 Elsevier B.V. All rights reserved.
doi:10.1016/j.ccr.2004.02.012

interaction of a molecule with a photon, accesses the ground and excited states of a molecular ion. In the simplest interpretation of a molecular PE spectrum these states correlate with holes in the occupied orbitals of the molecule. Thus, measurement of ionization energies gives a direct picture of the orbital structure of a molecule. Such experimental results have provided a challenge to electronic structure theory. Electronic structure calculations can be evaluated by how accurately they model a photoelectron spectrum.

All this may be achieved by the use of discharge lamps and without access to synchrotron radiation [2–4]. However, the ability to vary the photon energy in a PE experiment increases considerably its information content [5,6]. In addition to the binding energy information, which is independent of photon energy, a PE spectrum has intensity information. Band intensities vary with photon energy both in an absolute and in a relative sense. These changes are open to direct qualitative interpretation in terms of the atomic orbital (AO) contributions to the molecular orbital (MO) from which ionization is taking place [7,8]. Thus, with variable photon energy photoelectron spectroscopy there exists the potential for knowing the spatial distribution of the ionising electron. Such information produces a new challenge to theory. Calculation of ionization cross-sections involves modelling not only the originating orbital but also the ionising electron, which is computationally much more demanding. Successful calculation of cross-sections is important to give confidence in the detailed evaluation of the MO.

This article reviews the measurement, calculation and interpretation of PE energies and cross-sections of transition metal complexes in the gas phase. It aims to complement the preceding article [9] which addresses principally solid compounds and discusses in detail shake-up structure and electronic relaxation, which is not covered here.

2. Variable photon energy photoelectron spectroscopy

2.1. Measurement of photoelectron cross-sections

Synchrotron radiation provides an intense source of continuously tuneable highly polarized radiation that can be utilized in PE spectroscopy. The photon energy range of 15–150 eV is the most useful for the study of valence bands as it is within this energy range that the most significant variation in photon electron cross-sections occurs. As PE flux is a function of the angle of observation of the photoelectrons [10,11], measurements of band intensities are made at a “magic angle” where the intensity is independent of the angular parameter, β. The cross-section is then directly proportional to the band intensity [12]. Spectra are recorded at different photon energies and the intensities of the bands are measured as a function of photon energy. Such data can be used directly to obtain branching ratios, BR. These give the ratio of band intensities as a function of photon energy. To obtain cross-section data from the band intensity variations, instrumental factors such as the variation in photon flux and the sensitivity of the electron analyzer must be taken into account [13]. The former can be measured during spectral acquisition and other instrumental factors are normally adjusted for by calibration of the instrument with inert gases, whose absolute cross-sections have been accurately measured.

The process of extracting BR and cross-section data from a sequence of PE spectra is illustrated in Fig. 1. Spectra of $TiMeCl_3$ at three different photon energies are shown in Fig. 1a [14]. The relative intensity changes of the various spectral regions are very apparent and are quantified by fitting of Gaussians to the separate bands. The relative areas of these bands are plotted as BR in Fig. 1b; the sum of all the BR is one. The cross-sections of the bands are plotted in Fig. 1c, which shows how the intensity of each varies with photon energy.

In this review a number of studies have been selected to exemplify the field, others are not discussed. However, in Table 1 we have attempted to list the transition metal compounds that have been measured using synchrotron radiation in the gas phase. In some cases only spectra are reported, in other cases BR, and in others cross-section data. The principal restriction on the compounds is one of volatility; to obtain full cross-section data, vapour from the samples must be held at stable pressures over a period of days.

2.2. Qualitative interpretation of photoelectron cross-sections

The probability of photoionization to an ion state is proportional to the photoionization or photoelectron cross-section, commonly denoted $\sigma(\omega)$. Photoionization is a dipole transition between the initial and final states. The only difference from discrete electronic excitations is that the final state lies in the continuum. This means that for each energy $E > 0$ there is a solution of the Schrödinger equation. This solution does not decay at infinity, but oscillates periodically and corresponds physically to an electron asymptotically free. Moreover, each energy is infinitely degenerate, corresponding to the infinite choices for the direction of the photoelectron momentum, or equivalently for each value of the photoelectron angular momentum. For example, in the hydrogen atom, for each energy $E > 0$ there is a ψ_{Elmms} final orbital, that is an s-wave, a p-wave, and so on. Transition probability is controlled by the dipole transition moment

$$M_{\mathrm{f}i} = \langle \Psi_{\mathrm{f}} | r | \Psi_i \rangle \tag{1}$$

and the cross-section is proportional to the sum of the squares

$$\sigma \propto \sum_{\mathrm{f}} |M_{\mathrm{f}i}|^2 \tag{2}$$

over all final states available. Angular momentum and parity selection rules imply $l_{\mathrm{f}} = l_i \pm 1$, so for 1s ionization only

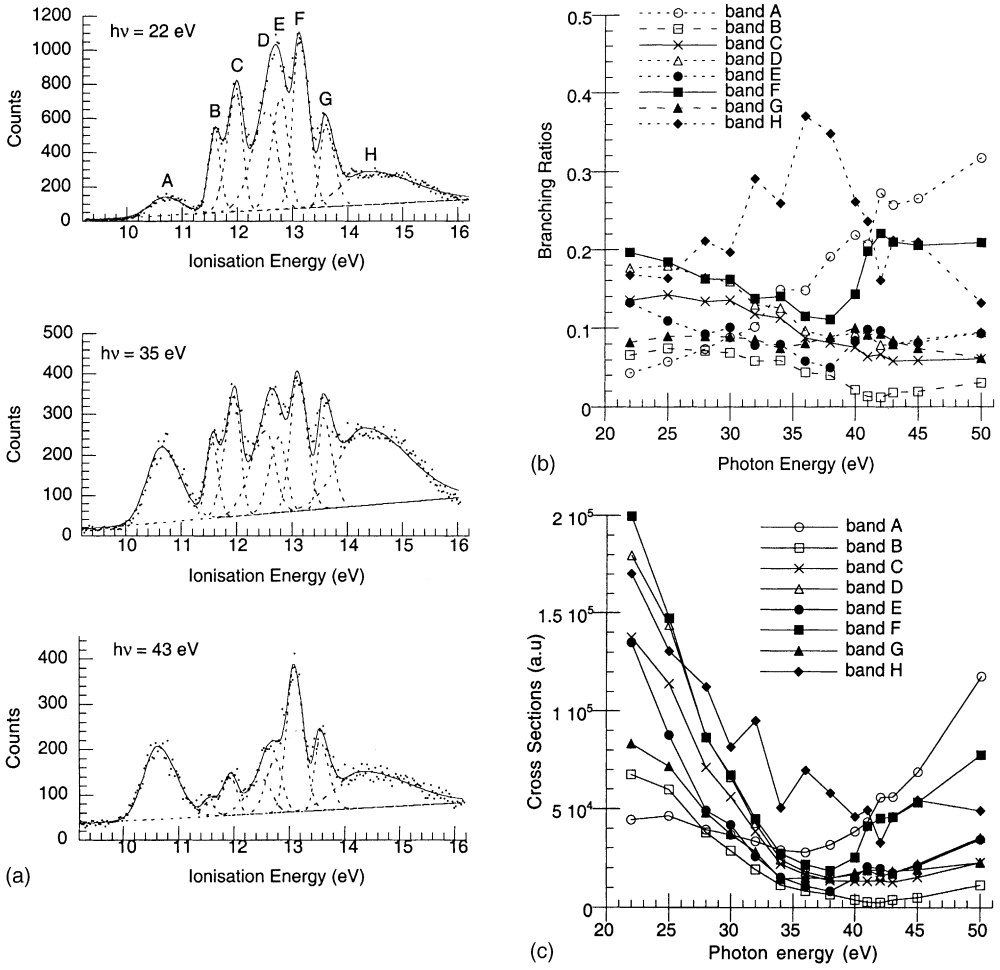

Fig. 1. (a) PE spectra of $TiMeCl_3$ at 22, 35 and 43 eV. (b) Branching ratios of valence bands of $TiMeCl_3$. (c) Cross-sections of valence band of $TiMeCl_3$.

the 1s → εp channel gives a contribution, while ionization of a 3d orbital occurs through the two channels 3d → εf and 3d → εp. Generally the $l \rightarrow l+1$ transition is the dominant contribution. The interaction, and hence the cross-section will be largest when the vacated orbital and the photoelectron wave are in the same spatial region. The variation of a photoelectron wave with photon energy gives rise to considerable variations in the cross-section.

In molecules, because of the loss of spherical symmetry, much more extensive mixing is possible, and interpretation is correspondingly more complicated. In favourable circumstances, the photon energy dependence of a band's cross-section is like a signature of the originating MO. The nature of that signature depends to a large extent on the type of AO that go to make up the MO. Thus, ideally, cross-section studies can provide a firm basis for band assignment and also reveal details of molecular bonding.

2.2.1. The Gelius model

The model on which most interpretations of molecular cross-sections are based is that of Gelius [7,8]. It makes a simplifying assumption that the cross-section for a MO is determined only by the cross-section of the atomic orbitals constituting the MO. The one electron cross-section, σ_j, for the jth MO is given by Eq. (3). The summation is carried out over all the AOs, χ_i^{A}, on the different atoms, A, which contribute to the MO, ϕ_j.

$$\sigma_j = \sum_{\mathrm{A},i} P_{j,i,\mathrm{A}} \sigma_i^{\mathrm{A}} \tag{3}$$

The σ_i^{A} are one electron atomic cross-sections and the $P_{j,i,\mathrm{A}}$ are factors describing the weight of the contribution of the AOs to the MO. In a LCAO MO treatment they are given by the squares of the coefficients $c_{j,i,\mathrm{A}}$ of the AO χ_i in the MO φ_j (Eq. (4))

$$P_{j,i,\mathrm{A}} = (c_{j,i,\mathrm{A}})^2 \tag{4}$$

The model is valid when the contribution of the overlap electron density to the cross-section is negligible and the effects of the anisotropy of the molecular ion potential on the outgoing electron wave function are small. Both these conditions are most likely to hold when the PE kinetic energy is high. At low photon energies molecular effects on ionization cross-sections are well documented, but even in these regions atomic effects are evident and the Gelius model pro-

Table 1
Transition metal compounds studied in the gas phase by synchrotron radiation

Compounds	Type of study[a]	Reference
Carbonyls		
$M(CO)_6$, M = Cr, Mo, W	V, BR, $\sigma(\omega)$	[13]
$W(CO)_6$	V, C	[68]
$Os(CO)_5$	C	[68]
$Os(CO)_4Pme_3$	V, C	[69]
$Re(CO)_5X$, X = Cl, Br, I	V, C	[68]
$Re_2(CO)_{10}$		
Sandwich molecules		
$M(\eta\text{-}C_5H_5)_2$, M = Fe, Ru, Os	V, BR, $\sigma(\omega)$	[23]
$M(\eta\text{-}C_5H_5)_2$, M = Cr, Co, Ni	V, BR, $\sigma(\omega)$	[33]
$Cr(C_6H_6)_2$ $Mo(C_6H_5Me)_2$	V, BR, $\sigma(\omega)$	[35]
$M(\eta\text{-}C_7H_7)(\eta\text{-}C_5H_5)$, M = Ti, Nb, Mo	V, BR, $\sigma(\omega)$	[34]
$Ta(\eta\text{-}C_7H_6Me)(\eta\text{-}C_5H_5)$		
$U(\eta\text{-}C_8H_8)_2$	V, BR, $\sigma(\omega)$	[22]
$M(\eta\text{-}C_3H_5)_2$, M = Ni, Pd, Pt	V, BR	[45,70]
$M(\eta\text{-}C_5H_5)(\eta\text{-}C_3H_5)$, M = Pd, Pt	V, BR	[71]
Half-sandwiches		
$Cr(\eta\text{-}C_6H_6)(CO)_3$	V, BR, $\sigma(\omega)$	[72]
$M(\eta\text{-}C_5H_5)(CO)_3$, M = Mn	V, BR, $\sigma(\omega)$	[72]
M = Mn, Re	V	[68,73]
$Ni(\eta\text{-}C_5H_5)(NO)$	V, BR, $\sigma(\omega)$	[39]
	V, BR	[40]
$M(\eta\text{-}C_5H_5)(CO)_2$, M = Co, Rh, Ir	V, BR	[68,74,75]
$Pt(\eta\text{-}C_5H_5)Me_3$	V, BR	[76]
$Pt(COD)Me_2$		
Tetrahedral molecules		
$TiCl_4$	V, BR, $\sigma(\omega)$	[31]
OsO_4	V, BR, $\sigma(\omega)$	[32]
$TiCl_3Me$	V, BR, $\sigma(\omega)$	[14]
ReO_3Me	V, BR, $\sigma(\omega)$	[77]
$Ni(PF_3)_4$	V, BR, $\sigma(\omega)$	[78]
Other systems		
$Mo_2(CF_3COO)_4$	V, BR, $\sigma(\omega)$, β	[51]
$Mo_4S_4(\eta\text{-}C_5H_4{}^iPr)_4$	V, BR, $\sigma(\omega)$	[79]
$Cu(CF_3CO_2CH)(CH_3)$	V, BR	[80]

[a] V: valence spectra presented; C: core spectra BR: branching ratios; $\sigma(\omega)$: cross-sections.

vides a good initial basis for molecular cross-section interpretation.

Thus, in order to evaluate the photon energy dependence of molecular cross-sections, some knowledge of atomic cross-section variations is required. Experimental data on atomic cross-sections is restricted but a useful compilation of calculated atomic cross-sections for direct photoionization exists [15].

2.2.2. Cross-sections of atomic orbitals

2.2.2.1. Decay of cross-section with photon energy. A cross-section is usually highest near the ionization threshold and after that decreases with increasing photon energy. As the kinetic energy of the photoelectron increases its wavelength decreases and the electron wave becomes more oscillatory. As a consequence, the positive and negative

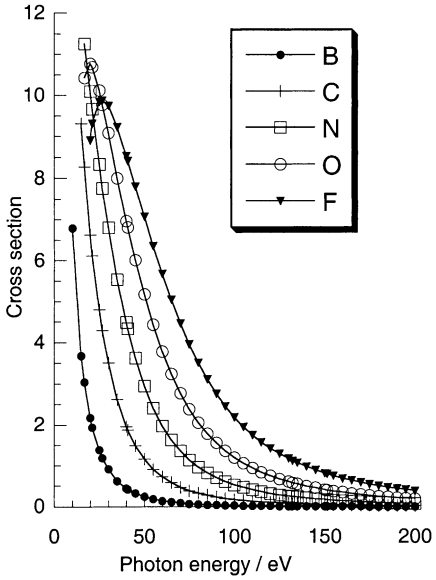

Fig. 2. Calculated 2p cross-sections (Mb) for the atoms B–F.

parts of the dipole matrix element with the vacated orbital tend to cancel one another, and the cross-section suffers rapid decay. The rate of decay can be characteristic of the AO ionized. The calculated cross-sections for the 2p orbitals of B–F are shown in Fig. 2 [15]. The more radially extended 2p orbitals of the lighter second period elements decay faster with photon energy than the contracted 2p orbitals of the more electronegative atoms.

2.2.2.2. Cooper minima. Other variations superimposed on the decay can also be characteristic. For orbitals with a radial node there is a minimum in the cross-section, known as a Cooper minimum [16,17]. At some photon energy the contributions from the inner and outer parts of the orbital will tend to cancel one another. The 3p cross-sections [15] calculated for Si to Cl show such minima (Fig. 3) which occur at increasing photon energies with increasing atomic number (Si 25 eV, P 30 eV, S 35 eV and Cl 40 eV). The consequent cross-section decay above threshold is very rapid and, although there are rises in cross-section at photon energies above the minima, the recovery is never such as to match the cross-sections of the 2p orbitals of second period atoms.

In the example of $TiMeCl_3$ (Fig. 1) bands B-E are assigned to Cl $p^{\cdot}$ lone pairs as their cross-sections decrease much faster with photon energy than that of band H which is C–H in origin.

2.2.2.3. Delayed maxima. Orbitals with high angular momentum, i.e. d or f orbitals, have maxima in their ionization cross-sections some way above threshold. This is in contrast to s and p orbitals where maxima, if they exist, tend to be very close to threshold. The effective potential experienced by an electron in an atom is given by the central field potential [18] and the radial wave equation is given by Eq. (5).

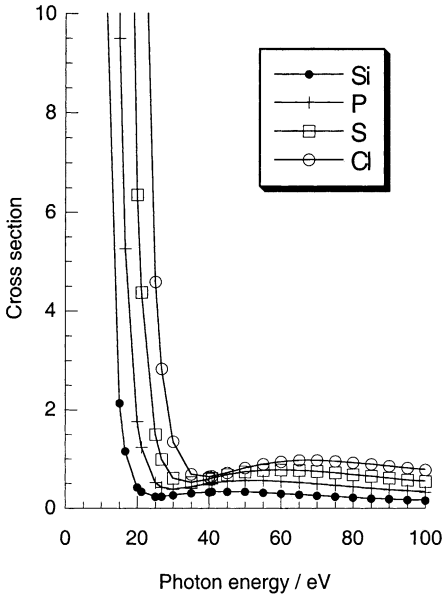

Fig. 3. Calculated 3p cross-sections (Mb) for the atoms Si to Cl.

$$\left[-\frac{1}{2}\frac{\mathrm{d}^2}{\mathrm{d}r^2}+\frac{l(l+1)}{2r^2}+V(r)\right]\psi_{nl}(r)=E\psi_{nl}(r) \quad (5)$$

$V(r)$ is the Coulombic potential of the nuclei and other electrons and $(l(l+1)/2r^2)$ is termed the centrifugal repulsion term and results from the solution of the angular part of the Schrödinger equation. For high values of l, the effect of the centrifugal term is to create a double well potential, which has an intermediate range maximum which may be positive. Fig. 4 illustrates the case for a bound f electron, which exists in the inner well, escaping as a g electron wave. At low photon energies the ensuing wave has insufficient energy to penetrate the centrifugal barrier so the interaction between the f electron and the g wave is small. At higher photon energies the interaction improves and the cross-section will pass through a maximum before decaying due to the normal oscillatory effects. In fact, the presence of a double well potential also for the continuum orbital gives rise to a shape resonance in the cross-section, due to formation of a quasi-bound eigenstate in the inner well, with much enhanced amplitude, over a small energy range. Both effects give rise to a maximum in the cross-section some way above threshold, but the shape resonance is characterized by a much sharper feature. Comparison of 3d and 4d ionizations in Kr and Xe, respectively, illustrates this point [19].

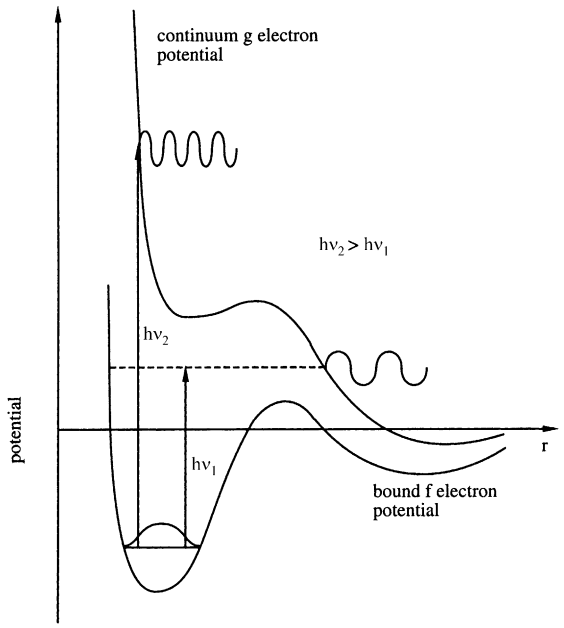

Fig. 4. Schematic representation of the double well potential experienced by a bound f electron and the potential of a g electron wane. Ionization at two photon energies $h\nu_1$ and $h\nu_2$ are shown.

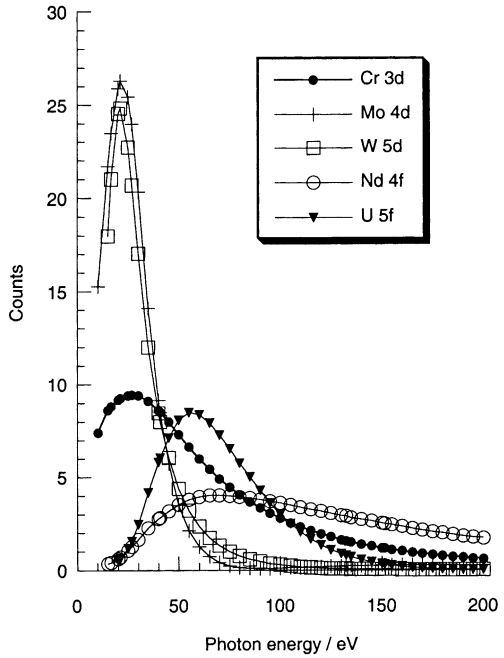

Fig. 5. Calculated $(n-1)$d cross-sections (Mb) for Cr, Mo and W and $(n-2)$ cross-sections (Mb) for Nd and U.

The calculated cross-sections for the valence d electrons of Cr, Mo and W and the 4f and 5f electrons of Nd and U are shown in Fig. 5 [15]. The maxima for the d electrons are at lower photon energy than the f as the angular momentum is lower and the centrifugal barrier less pronounced. It is also noteworthy that the Cooper minima in the cross-sections of those orbitals with radial nodes, i.e. 4d, 5d and 5f, cause them to decay faster with photon energy than the 3d and 4f orbitals which lack them.

2.2.2.4. Resonant enhancement of cross-sections. Perhaps the most dramatic departure from monotonic decay of a cross-section occurs for d and f electron cross-sections at photon energies near those necessary for excitation of particular core electrons.

In an independent particle picture one has a discrete state, like $3p^{-1}3d^{x+1}$, interacting with the continuum

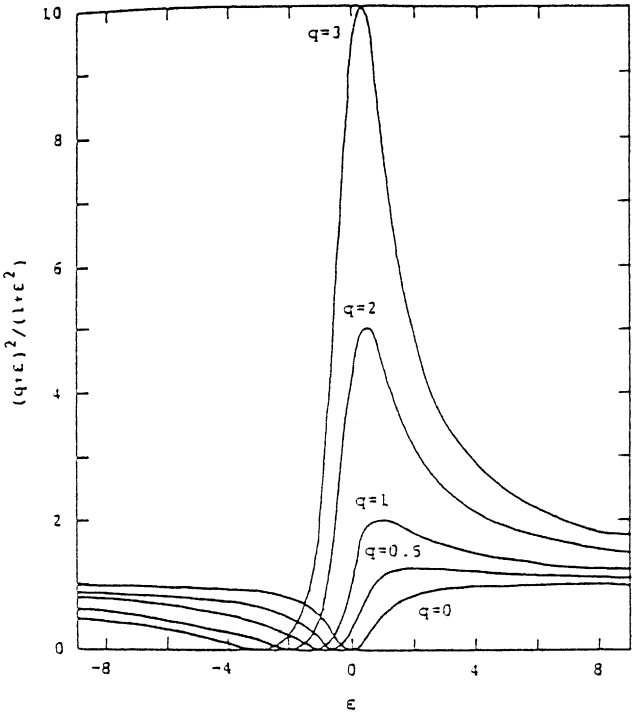

Fig. 6. Fano line profiles for different values of the shape parameter, q.

$3d^{x-1}\varepsilon f,\varepsilon p$. Configuration interaction mixes the discrete state, which loses its separate existence, in the continuum. The transition moment associated with the excitation into the discrete configuration, which can be very large if initial and final orbitals are strongly localized in the same region of space, e.g. 3p → 3d, interferes with that due to the original continuum, giving rise to sharp features in the cross-section, with the characteristic "Fano profile" [20,21] (Fig. 6). The strength of the resonance, and the shape of the profile, is governed both by transition moments, e.g. $\langle 3p|\mu|3d\rangle$, and the interaction between the discrete and continuum state, e.g. $\langle 3p^{-1}3d^{x+1}|1/r_{12}|3d^{x-1}\varepsilon f\rangle = \langle 3d3d|1/r_{12}|3p\varepsilon f\rangle$. This phenomenon is generally called autoionization, and, in particular for core excitation and decay all involving orbitals of the same principal quantum number, Super Coster Kronig (SCK) decay. This is possible in the case of d and f electrons, which give localized empty orbitals available for excitation because of the collapse into the inner potential well.

Resonance effects often dominate cross-sections over a wide range of photon energy. This is illustrated by the cross-sections found for ionization of the t_{2g}d electrons of the Group 6 hexacarbonyls [13] shown in Fig. 7. Substantial structure is seen in the cross-section plots of the $(n-1)$d electrons at and above the photon energy corresponding to the ionization energy of the core $(n-1)$p electrons in the metal atom.

Similar giant resonant enhancement of f electron cross-sections is also found. In these cases resonant excitation is from a core $(n-2)$d orbital to an empty $(n-2)$f orbital, and SCK decay involves repopulation of the core

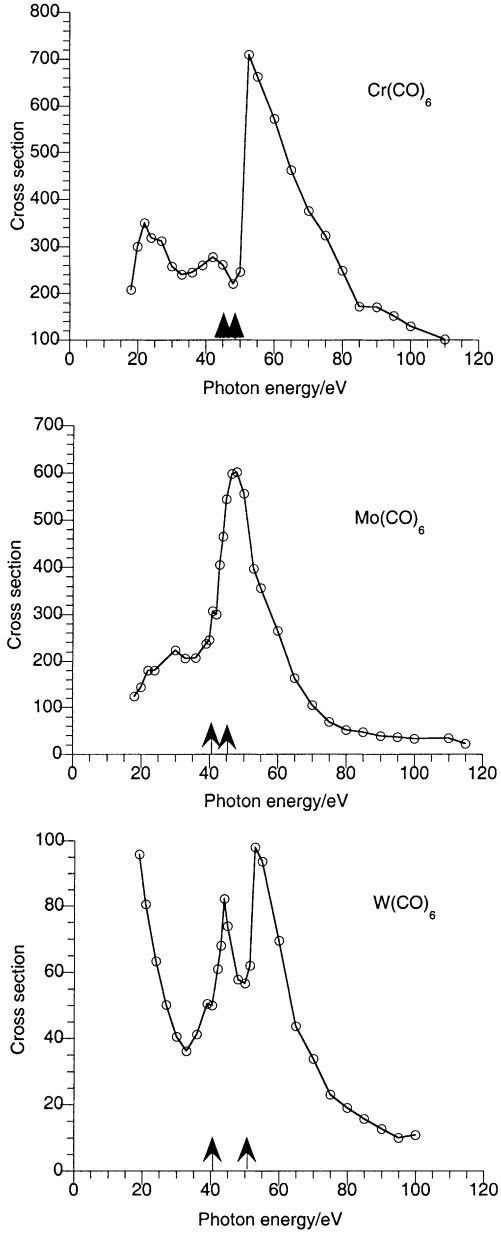

Fig. 7. Cross-sections of the t_{2g} d bands of $M(CO)_6$, M = Cr, Mo, W (arbitary units). The two arrows indicate the energies at which the core $(n-1)$p electrons ionize.

d hole and ejection of an f electron. For example the 5f band of $U(\eta\text{-}C_8H_8)_2$ shows two resonant features at photon energies between 90 and 110 eV [22] (Fig. 8); these photon energies are sufficient to excite the 5d core electrons. Both in the case of $W(CO)_6$ and $U(\eta\text{-}C_8H_8)_2$ the resonances show two maxima. The origin of this is spin–orbit splitting of the core hole.

The width of the cross-section resonances is substantial, spreading over many electron volts. Apart from the spin–orbit splitting mentioned above, for open shell systems exchange interaction between the core hole and the valence electrons can result in the spread of possible ex-

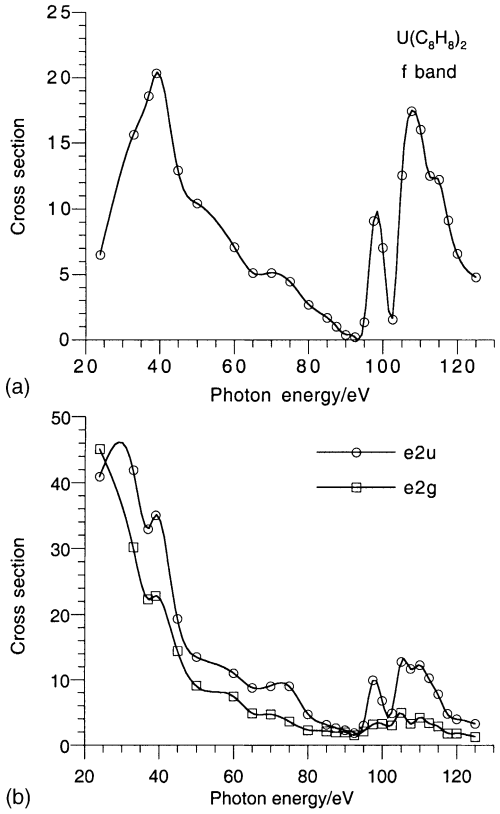

Fig. 8. Cross-sections of valence bands of U(η-C_8H_8)$_2$: (a) f band, and (b) e_{2u} and e_{2g} bands (arbitary units).

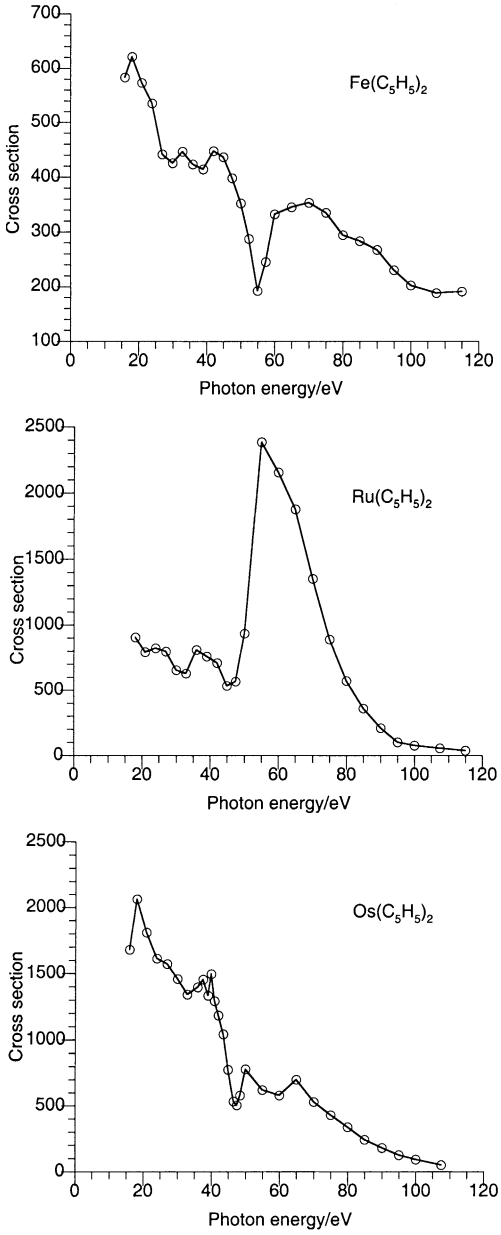

Fig. 9. Cross-sections of the d bands of M(η-C_5H_5)$_2$, M = Fe, Ru, Os (arbitary units).

cited states over a wide energy range, many of which lie above threshold for the excited electron. Resolution of both spin–orbit and exchange couplings is made difficult by the natural "line-widths"; as a result of the short lifetime of the excited state preceding SCK decay. The shape of the Fano profile depends on the relative strength of the two channels (Fig. 6). If the resonant channel is weak, enhancement may not occur, the shape parameter q is small, and the resulting profile is seen more as a dip in the cross-section. Three different types of profile seem to be evident for the metallocene triad, M(η-C_5H_5)$_2$, where M = Fe, Ru and Os [23]. Their d band cross-sections are shown in Fig. 9. For Fe there is a dip in the cross-section at 55 eV, for Ru strong enhancement is found with a small dip at 47.5 eV followed by a maximum at 55 eV, and for Os an intermediate situation exists with two minima at 47.5 and 60 eV and two weak maxima at 50 and 65 eV. Unlike cross-sections resulting from direct ionization, autoionization resonances have not yet proved tractable to calculation in such large systems, although they are within reach of approaches which include coupling between different channels, like RPA or TDDFT [24].

2.2.3. Molecular effects and shape resonances

Though many of the features of molecular PE cross-sections can be attributed to atomic effects, some features, such as shape resonances, are critically dependent on the form of the molecular potential [25–27]. This itself is determined in part by the physical shape of the molecule, from which the name of the effect derives. Shape resonances manifest themselves as increases in cross-section, which are frequently sharp and generally at relatively low PE kinetic energies. As has been mentioned in the atomic case, shape resonances are generally associated with the formation of quasi-bound states in potential wells generated by the charge distribution and the centrifugal barrier. Since the corresponding eigenstates are well localized within the molecular region the transition moment is correspondingly high giving the observed rise in the cross-section. In the molecular case, because of the three dimensional potential, it is difficult to predict systematically the appearance of shape resonances. Two popular models are trapping of

high angular momentum waves in the molecular potential [25], or excitations to highly localized anti-bonding orbitals located in the continuum [26], an example being the much studied σ_u resonance in N_2 [28], which is well described by an f-wave in a one-centre approach, or as a σ_u^* anti-bonding orbital in a minimal basis set LCAO model.

Additional resonances at higher energies may be associated with a diffraction effect, like in EXAFS, where an ionizing electron is scattered from neighbouring atoms, and so has maxima and minima in its amplitude as a function of its energy, as a result of the scattered waves reinforcing or interfering with the outgoing wave. In this model also, it is apparent that the resonances are a function of the shape and size of the molecule [29,30].

It has been observed empirically that the a_1 bands of tetrahedral molecules show shape resonances [31]. OsO_4 provides an example [32]. The $^2A_1$ band (Fig. 10a) shows a sharp rise in intensity around 52.5 eV. The cross-section plots (Fig. 10b) show that this is not associated with the 5p-5d resonance apparent in the $^2T_2 + {}^2E$ band. The resonance has an onset around the same photon energy and shows a double maximum expected for a third row transition metal. The related $^2A_1$ band of $TiCl_4$ shows a shape resonance at a lower photon energy of 40 eV [31].

Maxima in the PE ionization cross-sections of metallocenes and related sandwich molecules have been identified and assigned to shape resonances [23,33,34]. The molecular potential for this series of molecules is expected be

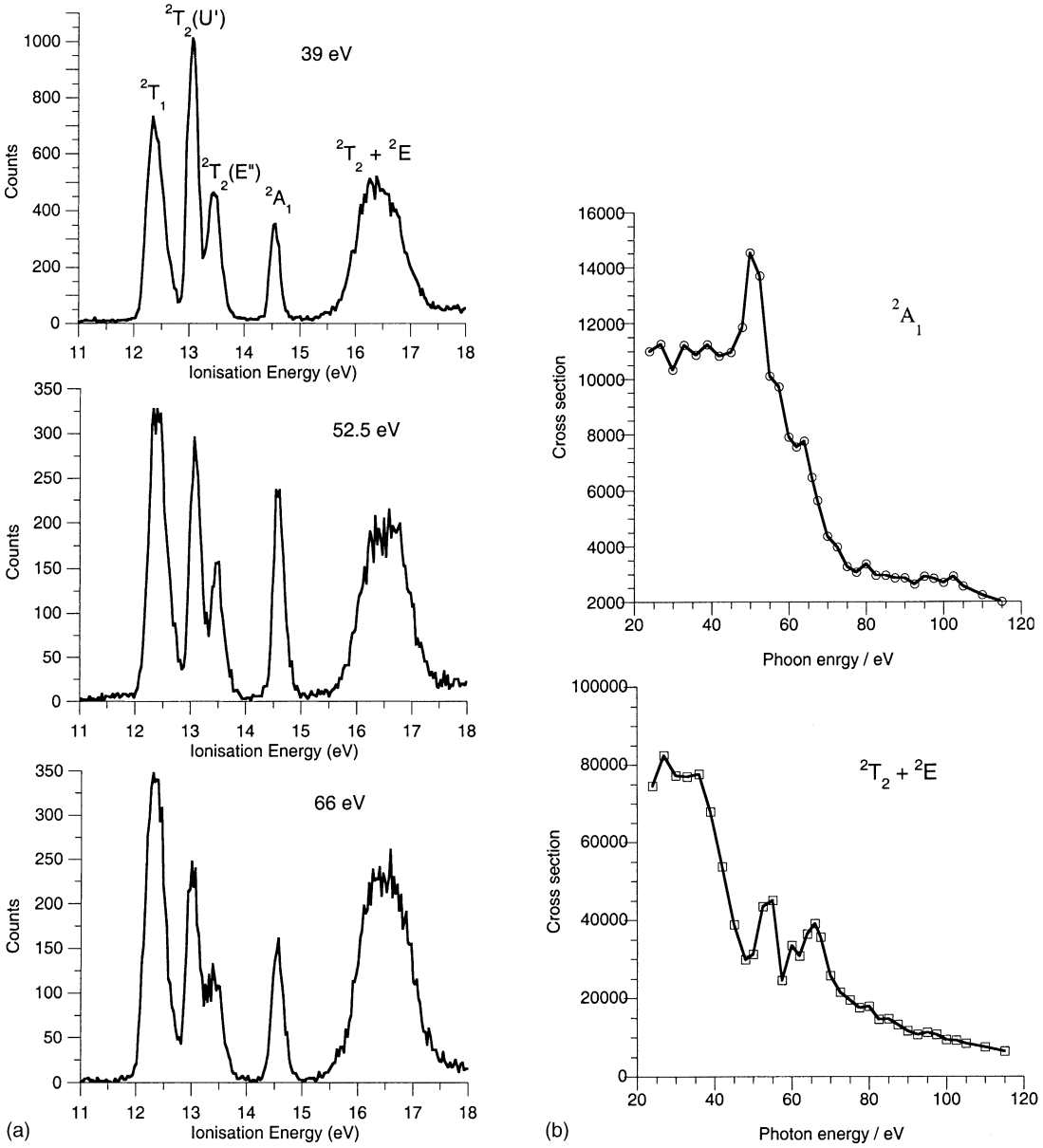

Fig. 10. (a) PE spectra of OsO_4 at photon energies of 39, 52.5 and 66 eV showing a rise in intensity of the $^2A_1$ band at 52.5 eV. (b) Cross-section of the $^2A_1$ band and the $^2T_2 + {}^2E$ bands (arbitary units).

very similar throughout the series and largely independent of the nature of the metal. For bis-cyclopentadienyl metal compounds a shape resonance occurs in a region between 36 and 40 eV, whereas the p → d resonances occur over a range of 43–75 eV depending on the metal. Bis-arene and cycloheptatrienyl–cyclopentadienyl compounds show similar features [34,35]. In the most part the shape resonances are most apparent in the metal based orbitals, the strength of the resonance increasing with the metal character. An exception to this is the ionization cross-section from the e_1'' HOMOs of cobaltocene and nickelocene [33]. These anti-bonding d orbitals show smaller p → d resonances than the more metal localized a_1' and e_2' orbitals, in accord with the expectation of their respective metal characters, but significantly stronger shape resonances.

These and other instances of the presence of shape resonances in the region of 40 eV photon energy provides a cautionary note for the interpretation of relative increases in band intensity in He II spectra, compared to He I spectra as attributable to metal d character.

2.3. Examples of PE cross-section analysis

Cross-sections have been used on a qualitative, semi-quantitative and fully quantitative level both to assign PE spectra and to make deductions about chemical bonding. Examples of all three types of analysis follow.

2.3.1. Assignment of bands and investigation of covalency

Detection of characteristic cross-section profiles may be used to assign bands to metal or ligand electrons. The presence of a giant resonance or a delayed maximum is particularly characteristic of metal electron cross-sections and has been illustrated for hexacarbonyls [13] (Fig. 7), metallocenes [23,33] (Fig. 9) and uranocene [22] (Fig. 8). Cooper minima are particularly useful in assigning ligand p bands such as those from the halides Cl to I [14,31] (Fig. 1).

Some cross-sections display a mixed signature with metal features superimposed on the general decay expected from a ligand band. In the spirit of the Gelius model, this is taken as an indication that they arise from an MO with both metal and ligand contributions, and thus are evidence for covalent interactions. A nice example of this is in the cross-sections of the second and third PE bands of U(η-C_8H_8)$_2$ [22] (Fig. 8). They both show a decay characteristic of C 2p based orbitals indicating localization of the electrons in the ring pπ orbitals. The second band shows a small d–f resonance indicating a U 5f contribution thus conclusively assigning this band to the e_{2u} orbital and giving elegant direct evidence of f orbital covalency in this molecule.

Bands A, F and G in the spectrum of $TiMeCl_3$ (Fig. 1) show a p–d resonance with a maximum at 43 eV even though this is a d^0 molecule [14]. This is due to the covalent character of the associated MO. Band A is assigned to ionization of the Ti–C bonding electrons and bands F and G to Ti–Cl bonding electrons.

2.3.2. Empirical analysis using the Gelius model

There are obvious difficulties attached to using the presence of atomic effects in molecular cross-sections in order to quantify the contribution of an atomic orbital to an MO. Calculations of atomic cross-sections are not precise for heavier elements and exclude giant resonance effects. The presence of shape resonances are not accounted for by the Gelius model. Inter-channel coupling may occur whereby final state ionization channels mix and borrow intensity from one another [5,36]. Nevertheless attempts have been made to deduce MO composition from PE cross-sections.

One such example concerns the compounds M(η^7-C_7H_6R)(η5-C_5H_5), R = H, M = Mo and Nb; R = Me, M = Ta [34]. They show four PE bands with IE below 10 eV; Fig. 11 shows the spectrum and the cross-sections for M = Mo. The assumption was made that band A was a purely metal based orbital and band D of 100% C 2p character. Weighted cross-sections of bands A and D were fitted to the cross-section of band B and the metal contribution to the MO giving rise to band B was deduced. This gave values varying between 60 and 70%. Subsequent DFT calculations [37], which gave good agreement with the IE, indicate a lower amount of metal character for these orbitals, 40%. Band A was calculated as around 90% d in character and bands C and D as around 85% ligand. Thus, qualitatively there is good agreement with the inference from the cross-section that the orbital giving band B is the main source of covalency, but quantitative agreement is not good.

2.3.3. Assignment using molecular cross-section calculations

Molecular cross-section calculations also suffer in comparison with experiment as they do not include effects of indirect ionization. However, where such resonances are small or can be excluded from the photon energy region under investigation, good agreement between experiment and theory has been achieved.

The PE spectrum of Ni(η-C_5H_5)(NO) provided an assignment challenge [38–40]. Four ion states were expected below 12 eV, two from e_1 orbitals, one from an a_1 orbital and one from a pair of e_2 orbitals. The a_1 and e_2 orbitals were expected to be mainly Ni 3d in character, whereas the e_1 orbitals encompass the principal interaction between the metal 3d(xz,yz) orbitals, the cyclopentadienyl e_1 orbital and the NO π anti-bonding orbitals. Four maxima are evident in the He I spectrum (Fig. 12a) and the original assignment was A_1 to $2e_1$, A_2 to a_1, B to e_2 and C to $1e_1$. The cross-section data on band B [39] (Fig. 12b) shows both that above 40 eV it becomes the most intense band and that, at 60–70 eV, there is a p–d resonance characterized by a Fano dip; both of these features indicate metal character. Band A has the most rapidly falling cross-section which indicates the least amount of Ni 3d contribution. Thus, a reassignment suggests itself whereby A_1 and A_2 constitute vibrational components of the $2e_1$ ionization, and band B comprises both the a_1 and the e_2 bands. This assignment is confirmed by molecular

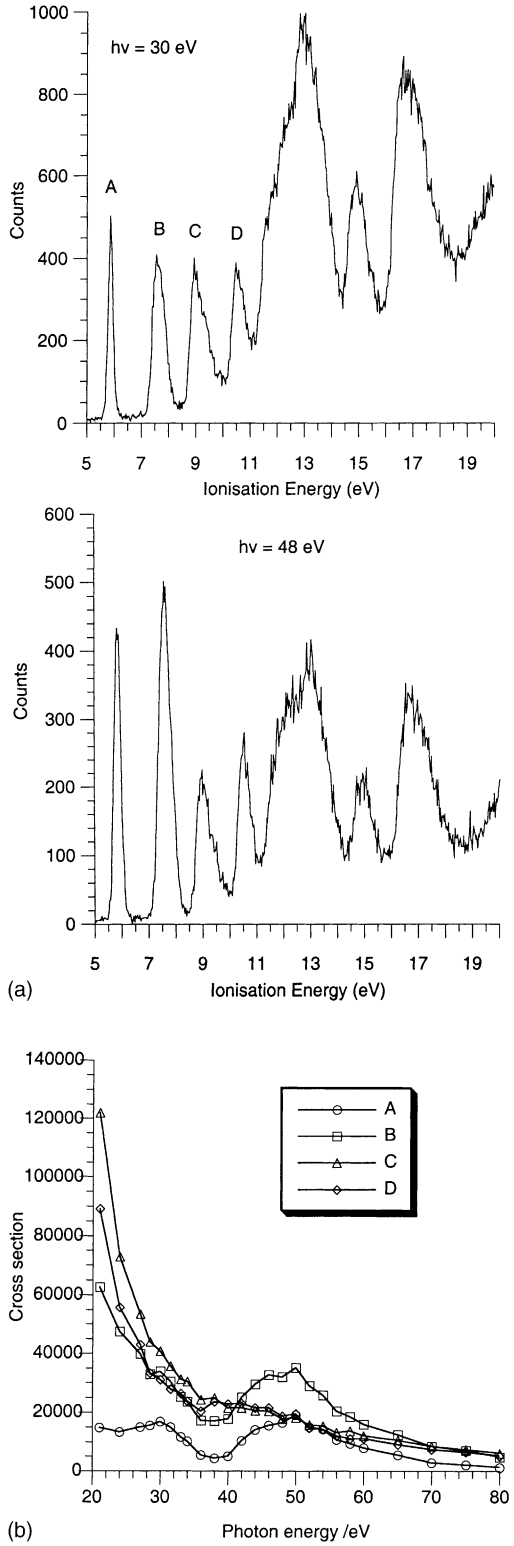

Fig. 11. (a) PE spectra of Mo(η-C_7H_7)(η-C_5H_5) at photon energies of 30 and 48 eV. (b) Cross-sections of bands A–D (arbitary units).

cross-section calculations [39] (Fig. 12c) between 18 and 52 eV, below the range of the resonance region. Excellent agreement between theory and experiment was found for the new assignment below 40 eV. Above 40 eV agreement was less good, but still better for the revised assignment than the original one.

3. Calculation of ionization energies

3.1. Ionization energies in ab initio and density functional theory

In ab initio theory, methods of calculating IE include the well known Koopmans' Theorem (KT) and ΔSCF (self-consistent field) approximations, the former obtained from a single SCF calculation of the ground state, the latter requiring a separate SCF calculation for each ionic state. The difference between the two calculated IE is termed relaxation energy, which always lowers the KT value. These methods may be refined by separate correlated calculation of the ground and ionic wavefunctions, thus obtaining correlated values of the IE's; correlation methods include configuration interaction (CI) or perturbation theory (PT) or a combination of the two, for example configuration interaction plus perturbative correction (CIPSI) or Complete Active Space Perturbation Theory at second order (CASPT2) methods [41,42]. Alternatively IE's can be obtained directly from the poles of the one particle Green's function (GF) (also called electron propagator) or from diagonalizing an effective operator in the very similar equation of motion (EOM) approach. The reader is referred to the Outer Valence Green Function (OVGF) approach, based on a renormalized third order PT expansion, and the ADC(3) approach (Algebraic Diagrammatic Construction (of the Green Function) at third order) [43], which is of comparable accuracy but preserves the correct analytical structure of the GF, and can be applied also when the former breaks down. Both relaxation and correlation effects in transition metal compounds often prove incredibly large in the ab initio framework. For instance in Ni(C_3H_5)$_2$ calculations give ΔSCF (KT) values of 7.30 (7.84) eV for the ligand $7a_u$ ionization and 5.71 (16.27) eV for the metal $9a_g$ one [44]. In fact the assignment of Ni(C_3H_5)$_2$ is still debated [45]. The behaviour is somehow erratic, since KT can offer a reasonable description of a PE spectrum, as in the case of $TiCl_4$ or $Ni(CO)_4$, or be totally useless, like in the former example. The worst problems seem associated with more covalent metal ligand bonding, and are probably due to an unbalanced description at the HF level of the larger correlation of the d shell with respect to that of s or p electrons. As a consequence, obtaining reliable IE's from ab initio methods may be very hard, and even generally accurate approaches, like ADC(3) may fail significantly.

A popular alternative is to employ DFT methods at the ΔSCF level. For numerical reasons the Slater transition state method has often been employed as a practical approximation to ΔSCF, although this is no longer needed and is just as computationally expensive. In any case the use of a density based exchange-correlation functional proves very suc-

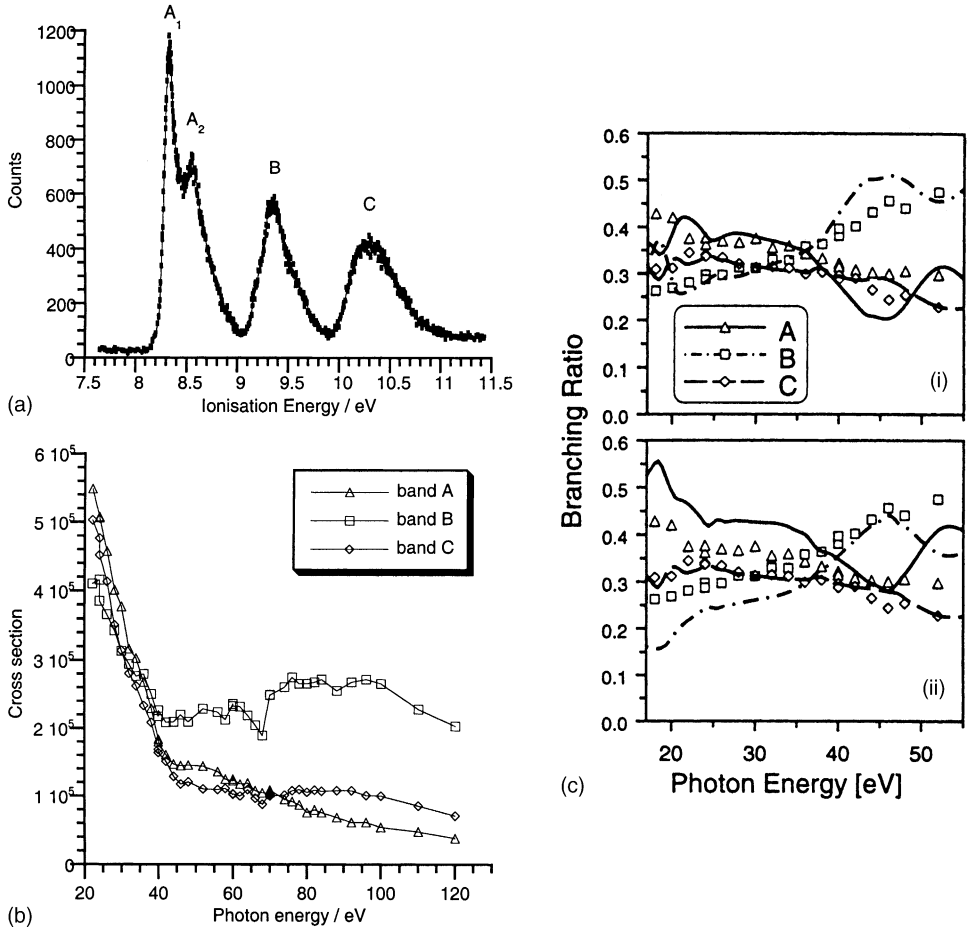

Fig. 12. (a) He I spectrum of Ni(η-C_5H_5)(NO). (b) Cross-sections of bands A–C of Ni(η-C_5H_5)(NO) (arbitary units). (c) Branching ratios for the first three bands of the photoelectron spectrum of Ni(η^5-C_5H_5)(NO) as obtained by LDKL-DF calculations compared to experiment: (i) assignment with band A comprising ionization from MO $2e_1$, B from MOs $a_1 + e_2$, and C from MO $1e_1$; (ii) previous assignment with band A comprising ionization from MOs $2e_1 + a_1$, B from MO e_2, and C from MO $1e_1$. Calculated results for bands A, B, and C are shown as lines (solid, dot-dashed, and dashed, respectively), measured results as symbols (triangles, squares, and diamonds, respectively).

cessful for reasons that are not entirely clear [46]. The advantage in transition metal compounds is probably due to a more uniform treatment of d and s, p correlation. However, also in small molecules like N_2, DFT is able to obtain the correct ordering of the ionic states, which is missed at both KT and ΔSCF *ab initio* levels. Given that DFT results are consistently quite satisfactory, the major drawback is that no systematic way of improvement is available when they are not. Moreover, problems are associated with the DFT treatment of states of multi-determinantal nature, like in the case of open shell ground state systems. A comparison of ab initio and DFT results for ferrocene is reported in Fig. 13.

3.2. IE of simple metallocenes

The metallocenes form useful benchmarks to test the quality of IE calculations and to illustrate the success of modern DF calculations to replicate vertical IE. Their PE spectra are reliably assigned and they provide a testing ground for the calculation of exchange splitting and spin–orbit coupling. The calculations reported here [47] were carried out using the ADF package [48] which enables fixing of the configuration, a considerable advantage when calculating excited states of a molecular ion. They employed Becke–Perdew gradient and correlation corrections (BP86) and triple zeta basis sets of Slater type orbitals with polarization functions on the main group atoms (TZP STO). For molecules and ions with unpaired spins the calculations were unrestricted. For the examples given, E states were described by a 0.5 occupancy of each orbital. Relativistic corrections were made using the zero order relativistic approximation (ZORA) formalism.

Fig. 13 provides a visual comparison of DFT methods and ab initio methods for ferrocene. Kohn–Sham one electron energies ($-\varepsilon_I$), IE calculated by the Slater transition state method (STS) and the ΔE method (direct calculation of the molecular ions in their ground and excited states) comprise the DFT methods [47] and KT, ΔSCF, and ADC(3) the ab initio ones [49]. The experimental vertical ionization energies for Fe(η-C_5H_5)$_2$ are also shown. For Ru(η-C_5H_5)$_2$ only experimental and DFT values are given [47]. Both the Slater transition state values and the ΔE values for the IE

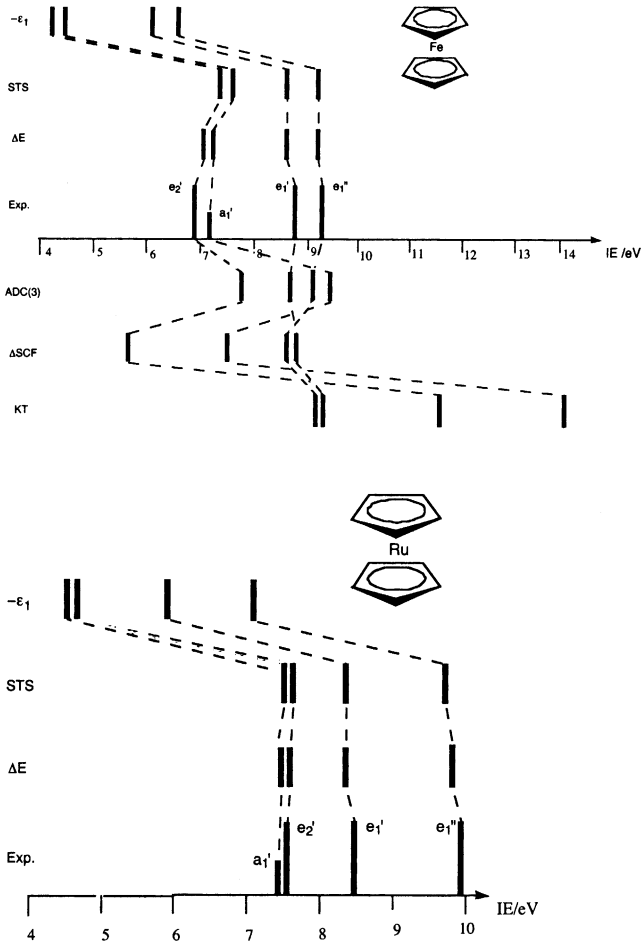

Fig. 13. Comparison of DFT methods (Kohn Sham orbital energies, $-\varepsilon_I$, IE calculated by the Slater transition state method, STS, and IE calculated by the ΔE method), ab initio methods (Koopmans' theorem, KT, ΔSCF and ADC(3)) and experimental vertical IE for Fe(η-C_5H_5)$_2$. Also DFT methods and experimental values for Ru(η-C_5H_5)$_2$.

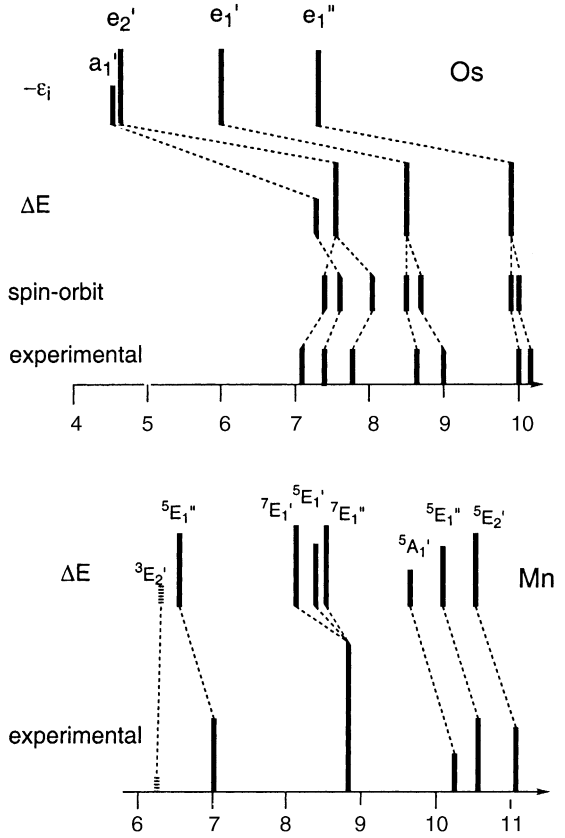

Fig. 14. Comparison of Kohn Sham orbital energies, $-\varepsilon_I$, IE calculated by the ΔE method and experimental vertical IE for Os(η-C_5H_5)$_2$ showing the effects of spin–orbit coupling and IE calculated by the ΔE method and experimental vertical IE for Mn(η-C_5H_5)$_2$ showing the effects of exchange splitting.

are in excellent agreement with experiment. What is also impressive is that the negative of the Kohn–Sham orbital energies, although about 3 eV less than the IE, have the same ordering and energy separations as do the ion states. Values from KT, ΔSCF and ADC(3) calculations described in Section 3.1 are erratic in their ion state ordering, and the values for the ligand based bands are significantly more accurate than those for the metal bands. The advantage of DFT methods in ion state assignment is evident throughout, and the numerical precision of the DFT ΔE method is impressive.

Fig. 14 shows comparisons between theory and experiment for Os(η-C_5H_5)$_2$ and Mn(η-C_5H_5)$_2$. In the case of Os(η-C_5H_5)$_2$, the $^2E_2'$ ion state is split by spin orbit coupling to form $J = 5/2$ and $J = 3/2$ ion states. Calculation on the ion states including spin–orbit coupling models the splitting well. The splitting of the $^2E_2'$ and $^2E_1''$ states are a consequence of their Os 5d orbital character, that of the $^2E_1'$ state is Os p orbital based, a d orbital contribution here is disallowed on symmetry grounds.

Calculation of exchange splittings is illustrated by the PE spectrum of Mn(η-C_5H_5)$_2$. Manganocene exists in the gas phase in a predominantly high spin form with $S = 5/2$. Ionization of the half-occupied d orbitals only give quintet states, but ionization from the doubly occupied ligand orbitals give rise to both quintet and septet states. The experimental and calculated values are represented in Fig. 14. Agreement is not as close here as in the closed shell molecules. The calculation suggests that the principal ligand band centred at 8.8 eV should be assigned to three of the ligand ion states, not four as previously thought. The $^5E_1''$ ion state arising from ionization of the e_1'' ligand orbitals is found at considerably higher IE than the other ligand bands. It has the same symmetry as the lowest accessible ion state from high spin manganocene which originates from a largely metal based ionization. Presumably strong interaction between these two ion states is responsible for the energy shift. One of the three bands in the 10–11 eV region was previously unassigned but can now be explained by the DFT calculation. At the temperature of the experiment some manganocene also exists in a $S = 1/2$ ground state. The triplet ground state of the associated ion, $^3E_2'$, can also be detected in the PE spectrum. The calculation shows good numerical agreement with the experimental

Table 2
Calculated and experimental ionization energies for ion states of OsO_4

Ion state (orbital)	Calculated IE DV-Xα	Calculated IE ADF	Experimental IE
$4U'$ ($1t_1$)	13.44	12.73	12.35
$2E'$ ($1t_1$)	13.55	12.75	
$3U'$ ($3t_2$)	14.12	13.20	13.11
$1E''$ ($3t_2$)	14.57	13.27	13.54
$1E'$ ($1a_1$)	14.86	14.89	14.66
$1E''$ ($2t_2$)	17.55	16.78	16.4–16.8
$2U'$ ($2t_2$)	17.75	16.86	
$1U'$ (1e)	18.50	17.42	

value for this state but underestimates the separation with the $^5E_1''$ state of the predominant ion species. However, DFT as yet is unable to predict the correct ground state for $Mn(\eta\text{-}C_5H_5)_2$ as it estimates the doublet state to be more stable than the quintet. As DFT is increasingly used to argue the relative stability of spin states in metallo-enzymes, progress is needed in improving the accuracy of exchange stabilization calculations.

OsO_4 provides a further example of calculation of spin–orbit coupling [50]. The cross-sections showed that the only orbitals with substantial d character were those giving rise to the band at 16.5 eV (Fig. 10). Also calculations strongly suggested that this band must accommodate both the $^2T_2$ and ^2E ion states. This led to the necessity of assigning the second and third band to the U' and E'' spin orbit components of a split $^2T_2$ ion state. However minimal d content of this orbital, demonstrated both experimentally and computationally, and the $U' < E''$ ordering suggested the origin of the splitting must be Os p based [32]. The size of the splitting was difficult to explain on the basis of the small amount of 6p character but calculation including the Os 5p core electrons gave satisfactory agreement with experiment (Table 2).

4. Calculation of cross-sections

Although many aspects of molecular cross-sections are well understood qualitatively, a quantitative theoretical model can be useful in several respects:

(a) Assignment of a photoelectron band to ionization from a specific orbital, by comparison of the experimental and theoretical profiles. An example has already been considered for $Ni(\eta\text{-}C_5H_5)NO$ [39].
(b) Clarification of the origin and nature of the features in the profiles (maxima, minima, specific shapes), and in particular resonances, by analysis of the wavefunction at the corresponding energy. This may be particularly helpful to correlate the cross-section features to the underlying geometrical and electronic structure, notably to aid interpreting the evolution of such features along series of chemically related compounds, substituent effects, and so on.
(c) Assistance in maximising the quantitative information from the experimental data. Since interpretation of the features requires an underlying model, its availability allows more significant quantitative information to be extracted from the experimental data. A possible example may be the monitoring of the AO composition of the relevant molecular orbital (degree of covalency) refining the Gelius model, which is a bit too crude to be widely applicable in a quantitative way, especially in the interesting low energy range. While precise numbers are to be determined from the experimental data, a realistic and computationally tractable theoretical model can also provide means to characterize more quantitatively features present in the experimental profiles.
(d) Finally a second dynamical observable in photoelectron spectra is the asymmetry parameter β which characterizes the photoelectron angular distribution. The measurement of β is more delicate and time consuming, so very little has been done experimentally in the field of transition metal compounds. However it is an important observable, since it is often sensitive to features of the wavefunction complementary to those affecting cross-sections, and correspondingly weak features in σ can be prominent in β and vice versa [51]. Therefore, β can also be an important probe of the geometric and electronic structure. Though its interpretation is even more difficult than that of cross-sections, theoretical methods able to obtain the final continuum wave-function can obtain β without additional effort. Recent results by the present approach compared to experimental results are available in the literature for the hydrides [52,53], N_2 [54], CO [55], and C_6H_6 [56].

4.1. Continuum wave-functions

Theoretical ingredients for the calculation of cross-sections are transition dipole moments (1) between the initial bound state and continuum wavefunction Ψ_0 and Ψ_E (and the phase shifts, which characterize the asymptotic behaviour of Ψ_E, for the calculation of β). Since computational models for the determination of the bound wavefunction are much more advanced than those for Ψ_E, we focus on the latter. Because of the complexity of transition metal compounds, it will be difficult to go beyond simple approximations for the wavefunction, in particular beyond the level of single particle excitations. More correlated approaches are available for small molecules but shall not be considered here. The models available are as follows.

4.1.1. Independent particle models

A single determinant is employed for the initial and final wavefunctions

$$\Psi_0 = |\varphi_1, \ldots, \varphi_i, \ldots, \varphi_N\rangle$$

$$\Psi_{Ei} = |\varphi_1, \ldots, \varphi_{Ei}, \ldots, \varphi_N\rangle$$

Corresponding to the single particle excitation $\varphi_i \rightarrow \varphi_{Ei}$

One can use either the Hartree–Fock approach (also called static exchange, SE) or a density functional approach (the Kohn–Sham Hamiltonian, KS).

4.1.2. Coupling of single particle excitations

The final state wavefunction is a mixing of the previous independent particle functions

$$\Psi_{Ej} = \sum_i C_{ij} |\varphi_1, \ldots, \varphi_{Ei}, \ldots, \varphi_N\rangle$$

Depending on the precise scheme there are several approaches like SCI or TDA, RPA, TDDFT (time dependent density functional theory). At this level both interchannel coupling, which transfers intensity from one channel to another, and singly excited autoionizations, like 3p → 3d or 4d → 4f SCK giant resonances are included.

Central to both approaches is the solution of a single particle Schrödinger equation in the continuum. It is now possible to solve such equations efficiently, without further approximations, like the Muffin Tin approximation in the

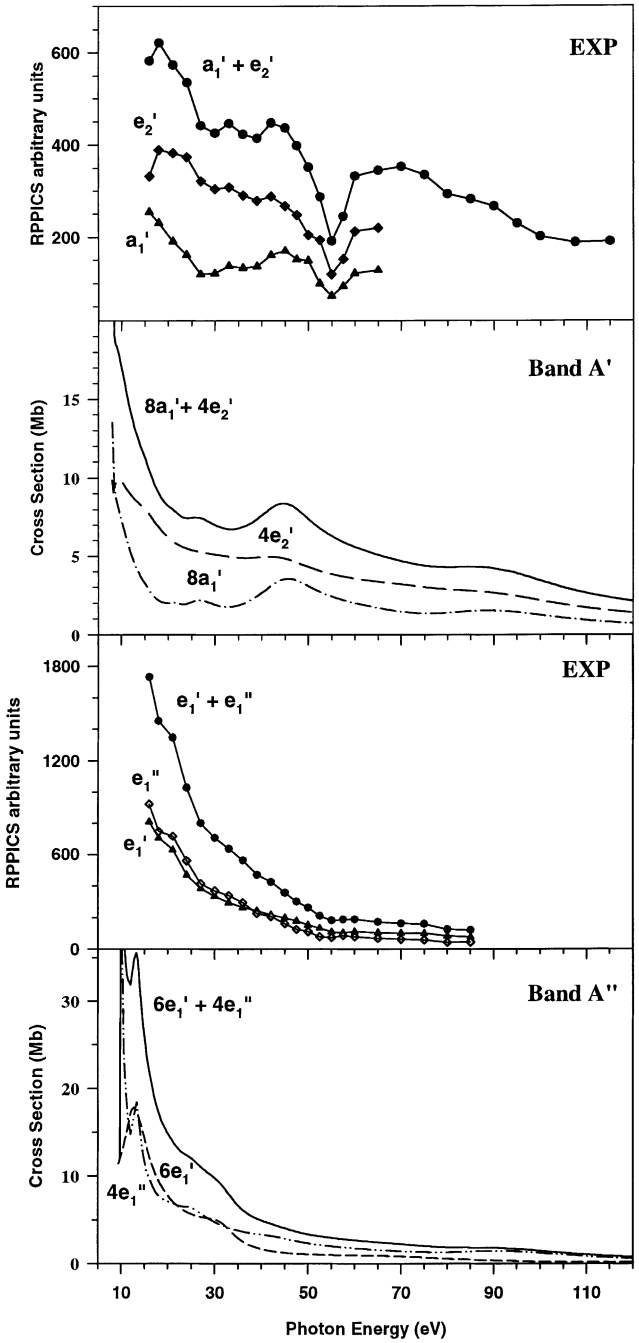

Fig. 15. Experimental (upper panel) and calculated cross-sections (lower panel) of the bands A′ ($4e_2'$ and $8a_1'$ ionizations) and A″ ($6e_1'$ and $4e_1''$ ionizations) of $FeCp_2$.

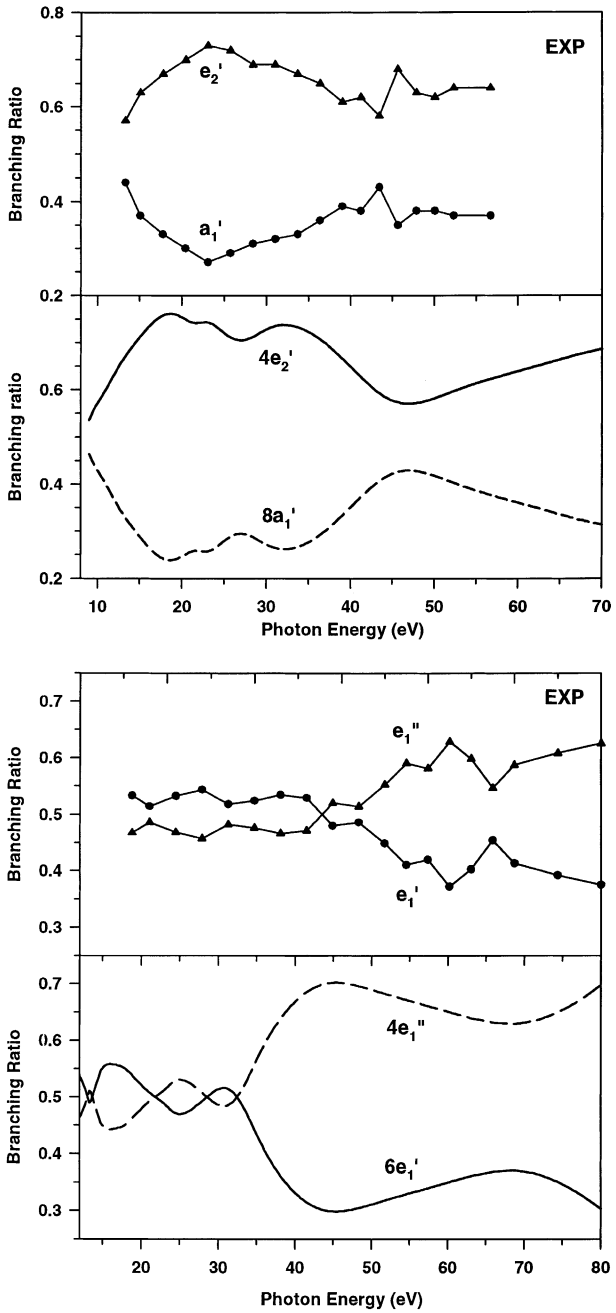

Fig. 16. Experimental (upper panel) and calculated branching ratios (lower panel) of the bands A′ ($4e_2'$ and $8a_1'$ ionizations) and A″ ($6e_1'$ and $4e_1''$ ionizations) of $FeCp_2$.

well known Multiple Scattering approach. Details of the present approach are given in the literature [57,58].

A few results are illustrated below. Only KS results are presently available for organometallic systems, but it is expected that TDDFT calculations [54], which are more accurate and should be able to describe SCK resonance features, will be feasible in the near future. All results reported are at fixed equilibrium geometry and neglect any nuclear motion effect. Ground state wavefunctions are computed with the ADF code [45,59] employing internal DZP STO bases and the LB94 exchange-correlation potential [60].

4.2. Cross-sections in the metallocenes

A good illustration of present capabilities is photoionization of ferrocene. The spectrum shows four individual bands, $4e'_2$(3d), $8a'_1$ (3d), $6e'_1$ (π), $4e''_1$ (π), followed by more ligand bands, B and C, at higher IEs, comprising several ionizations [3,23]. Covalency is expected in $4e'_2$ (d → π* back-bonding) and especially $4e''_1$ (π → d bonding). Experimental and calculated [61] cross-section profiles are presented in Fig. 15, and branching ratios in Fig. 16. BR including also B and C bands are reported in Fig. 17. A comparison of β values for the first four bands is presented in Fig. 18.

Since the basic features and their physical origin have been already discussed we just summarize the main points specific to the theoretical results.

The general agreement between experimental and theoretical values is very satisfactory, already at the simple KS level employed. There is still room for improvement at the KS level, by refining the exchange correlation potential, before employing the more demanding TDDFT approach. With the only exception of the SCK resonance feature, which is missed at the KS level, all other features are at least qualitatively well reproduced, and also the quantitative agreement is fairly satisfactory. The first aim of the theoretical approach, to provide a firm basis for band assignment, appears thoroughly achieved. In the case of ferrocene, interpretation of the experimental features provides already overwhelming evidence for the proposed assignment [3,23], although that was questioned by high level ab initio calculations of the IEs only [49]. The agreement between the

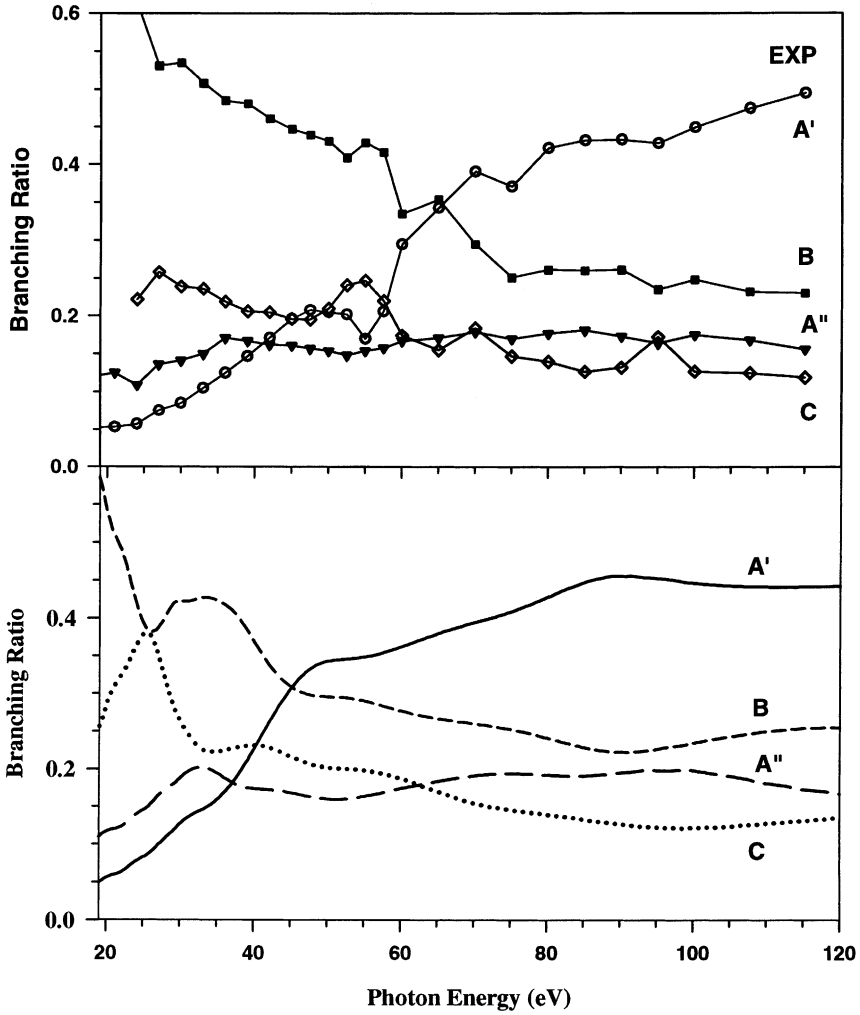

Fig. 17. Experimental (upper panel) and calculated (lower panel) branching ratios of the valence bands of $FeCp_2$.

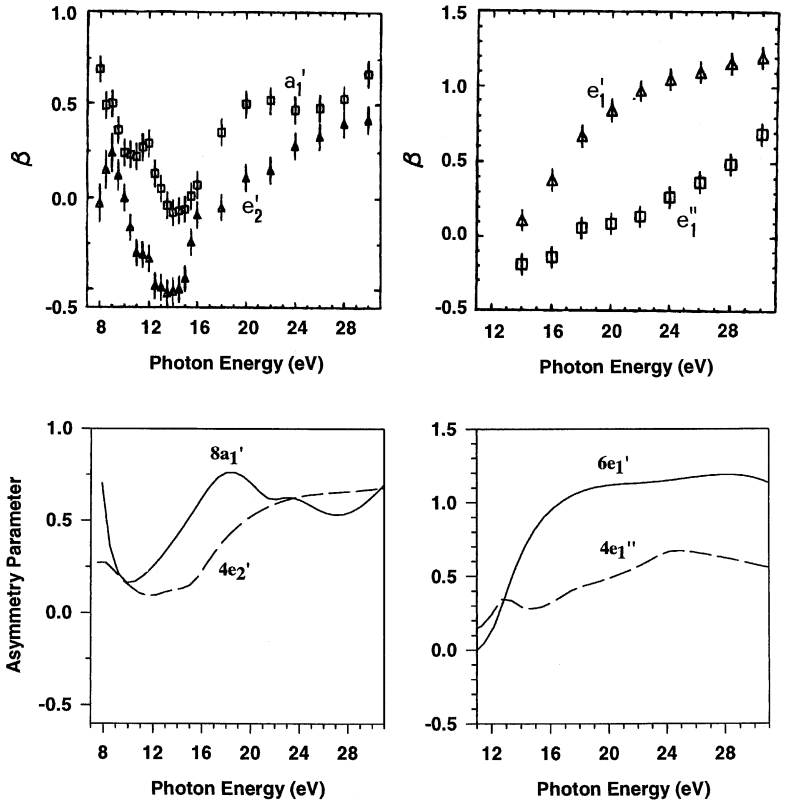

Fig. 18. Experimental (upper panel, ref. [6]) and calculated (lower panel) asymmetry parameter β of the bands A′ ($4e'_2$ and $8a'_1$ ionizations) and A″ ($6e'_1$ and $4e''_1$ ionizations) of $FeCp_2$.

experimental and calculated profiles for σ, β and the BR is such that in the absence of any previous interpretation the assignment of the experimental spectrum on the basis of the calculated profiles alone is definite. As an example consider the two π orbitals $4e_{1g}$ and $6e_{1u}$ in $Cr(\eta\text{-}C_6H_6)_2$, which correspond to the $4e''_1$ and $6e'_1$ in $Fe(\eta\text{-}C_5H_5)_2$. They lie unresolved and probably very close under a single experimental band [3,35]. It is assumed that $4e_{1g}$ has the higher IE, being the metal bonding orbital, in analogy with $Fe(\eta\text{-}C_5H_5)_2$. Actually DFT eigenvalues show the opposite order, due to the large anti-bonding interaction between the π orbitals of the two rings. A possible solution could be slicing the experimental band at the low and high binding energy side, and considering the BR or β profiles, as was done successfully to identify the relative position of the n and π ionizations in pyridine long ago [62]. The calculated BR is reported in Fig. 19, while β profiles are published [63].

As concerns the precise identification of the features present in the cross-section profiles, it is clear that they are many, often overlapping, and that experimental data alone offer limited means of characterizing them. Let us analyse a single point, shape resonances. A shape resonance is a "quasi bound" state due to the shape of the potential well. Due to the complexity of the molecular potential it is however difficult to ascertain the nature of the resonance. A primary aid from the theoretical results is the decomposition of the cross-section in separate contributions from the different

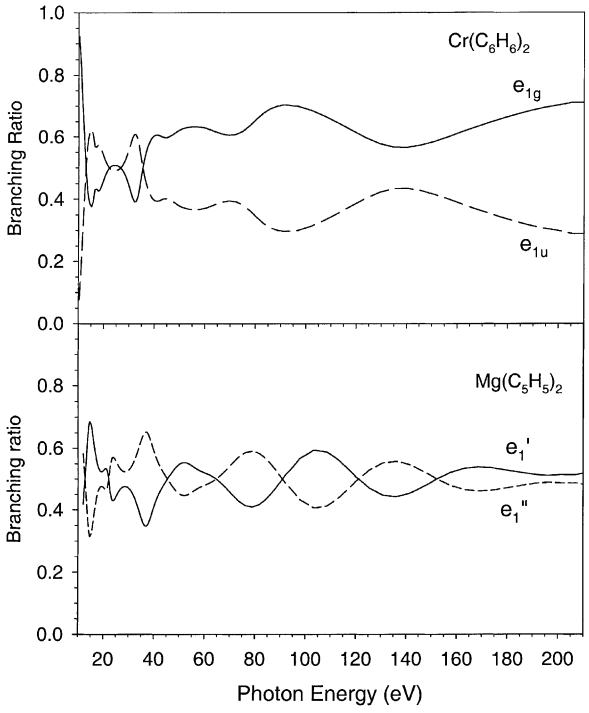

Fig. 19. Theoretical branching ratios relative to the ligand π ionizations of $Cr(\eta\text{-}C_6H_6)_2$. (upper panel, $4e_{1g}$ and $6e_{1u}$ ionizations) and of $Mg(\eta\text{-}C_5H_5)_2$ (lower panel, $5e'_1$ and $4e''_1$ ionizations).

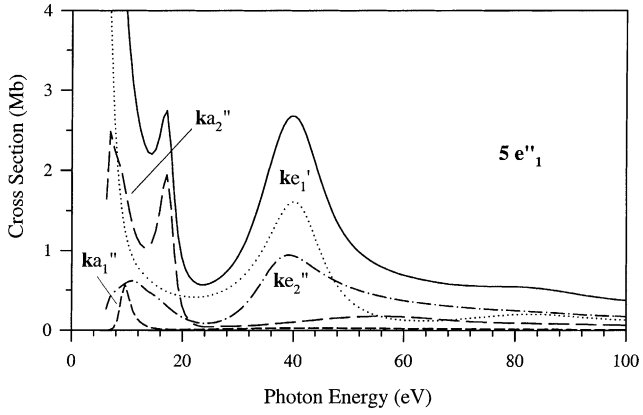

Fig. 20. Calculated cross-section profiles and partial channel contributions relative to the $5e''_1$ ionization in Co(η-C_5H_5)$_2$.

final channels available. This is reported in Fig. 20 for the outermost ionization $5e''_1$ of Co(η-C_5H_5)$_2$ [64]. Clearly the big shape resonance at 40 eV is mainly due to the ke'_1 (and ke''_2) final channels, while the narrow structure at 17.11 is entirely ascribed to the ka''_2 one. Actually, despite the large degeneracy in the continuum, it is possible to form a correctly normalized component which carries all the transition moment, the so called "dipole prepared" state [64,65]. In this way it is possible to plot and analyze a single final continuum state. An example is reported in Fig. 21 relative to the $5e''_1 \rightarrow ke'_1$ channel. The ke'_1 continuum is plotted at four photon energies corresponding to the two maxima in the cross-section at 8.27 and 40.24 eV and two minima at 21.88 and 65.42 eV, respectively. It is seen that the continuum starts as a p_x wave at the metal, as indicated by the large amplitude and nodal structure at the origin. Then it becomes de-

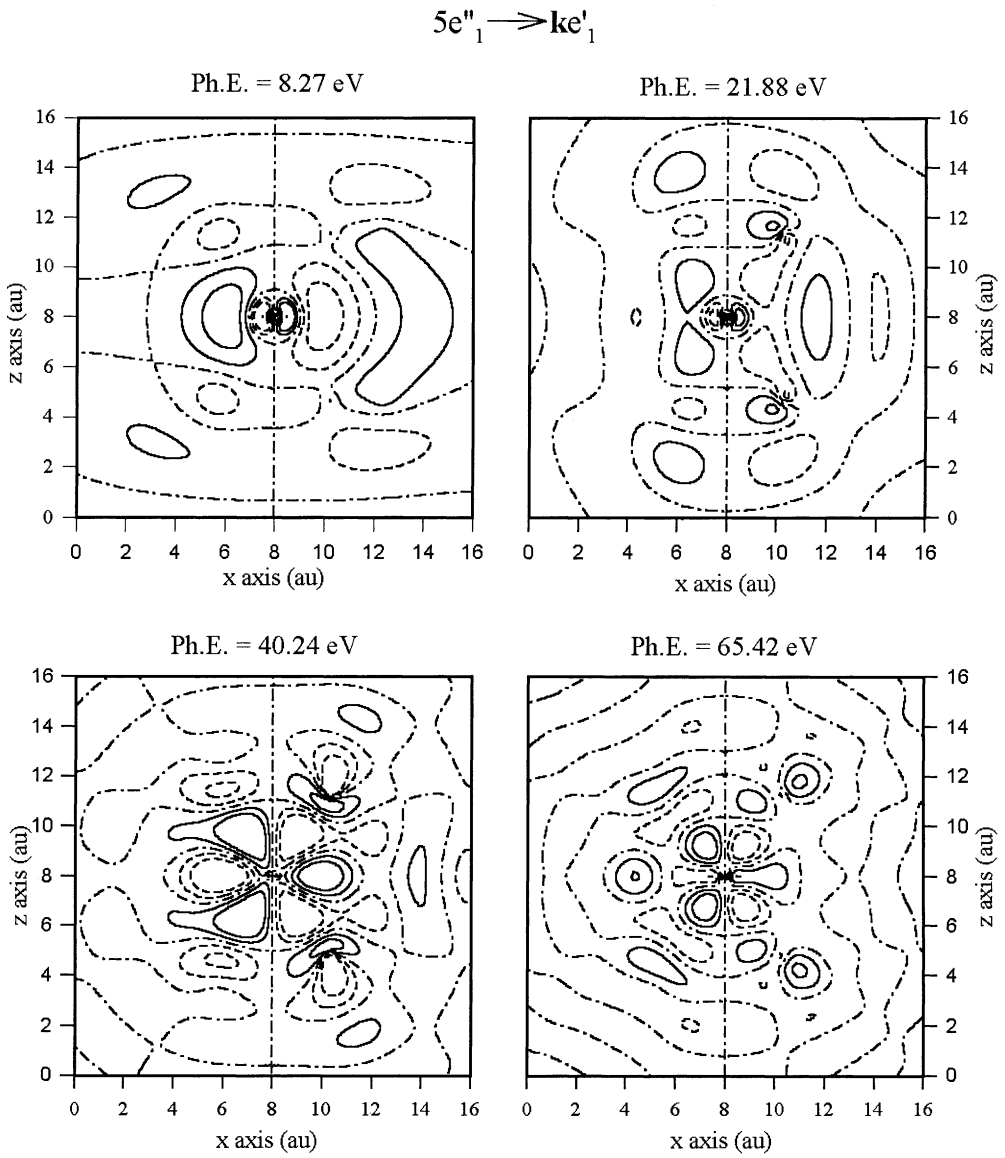

Fig. 21. Contour plots of the final continuum orbitals for the $5e''_1 \rightarrow ke'_1$ ionization channel at selected photon energies for Co(η-C_5H_5)$_2$ (Ph.E. is photon energy).

localized at higher energies (corresponding to the first minimum) since the isolines become sparser and shift towards the rings. At the resonance energy it is again dominated by an f(xz^2) wave, well localized inside the cage, that slowly delocalizes and fades away at higher energy. The same analysis shows that the feature computed at 17 eV in the ka_2'' channel is due to a trapping of a p wave inside the cage (a metal $4p_z$ resonance). So it appears that virtual metal 4f and 4p valence type orbitals, which cannot be supported by the neutral atom potential, become available as resonances in the additional potential generated by the ligand cage.

Quantifying covalency in metal–ligand bonding has been already considered by analysis of the experimental cross-sections based on the Gelius model, but has met limited success, essentially because of the crudeness of the model, or put another way, the wealth of molecular features superimposed on pure atomic behaviour. This is apparent from the BR of the π_+–π_- ligand bands in Fe(η-C_5H_5)$_2$ (Fig. 16), and Mg(η-C_5H_5)$_2$, Cr(η-C_6H_6)$_2$ (Fig. 19). Covalency is clearly indicated by the BR of the $4e_1''$ band in Fe(η-C_5H_5)$_2$, which at higher energy becomes much larger than 0.5, the value to be expected for pure ligand ionization. The same is apparent for the $4e_{1g}$ in Cr(η-C_6H_6)$_2$, although the deviation is notably reduced. Indeed in Mg(η-C_5H_5)$_2$ the BR of both $5e_1'$ and $4e_1''$ oscillate around 0.5, because of the low cross-section of Mg 3p orbitals and the more ionic character of the bonding. Of course care has to be exercised when comparing orbitals from different ligands (C_5H_5 and C_6H_6) and with different metals. What is more important and perhaps unexpected is the persistence of molecular features, seen in the oscillations of the BR, even at high energies. The value of a theoretical model is twofold. Firstly, it can more easily employ alternative decompositions of the cross-sections, for instance employing well defined fragments, like the (η-C_5H_5)$_2$ or (η-C_6H_6)$_2$ cages, that can be separately computed. An attempt to decompose total cross-sections into contributions of functional groups has recently been presented by Lichtenberger et al. [66] Secondly, it can test the validity of the various models purely within the theoretical data. For instance the Gelius model can be explored purely theoretically, for its ability to fit the computed cross-sections. Then, after subtracting the molecular features one could make best use of the rather small differences between different compounds. Thirdly, the real numbers quantifying the effect can be extracted from the experiments. As a final comment of the benefit of a theoretical model is the ease with which different systems can be investigated, offering the possibility of a pre-screening of potentially interesting effects, directing experiments towards the most promising targets.

5. Summary and conclusions

Photoelectron cross-sections show a great variety of phenomena which are well understood in physical terms. Such experimental data contain a large quantity of information relevant to structure and bonding. However, reliable extraction of this information requires a good theoretical model and accurate modelling of the cross-sections. Current theory is able to get most features qualitatively correct, and, given the challenge of describing an ionized electron in the field of a molecular ion, is also quite successful quantitatively. Closer interaction between theory and experiment should increase understanding of individual details.

A number of topics have been barely touched or altogether neglected. A short list comprises:

- Asymmetries in the angular distributions. In addition to the dipolar parameter β, further asymmetries arise in chiral molecules, characterized by a dichroic parameter D, which opens an important field in the study of chirality, or as a contribution of the multipolar moments of the radiation field, which could probe additional details of the electronic distribution.
- Relativistic effects on cross-sections, like branching ratios between spin–orbit components, and spin polarization effects.
- Multiplet effects in open shell systems, which are quite common in transition metal chemistry, like dynamical effects on branching ratios.
- Description of satellite states, and the very large correlation effects often found in transition metal compounds, their dynamical behaviour, and signatures of correlation effects on cross-sections and angular distributions.
- Vibrational and vibronic effects, and dynamical behaviour of individual vibronic components.
- Quantitative analysis of features in the PE spectra, like shape and autoionization resonances. Evolution of the features in series of related compounds, to exploit the sensitivity to changes of the molecular potentials induced by the chemical environment, chemical shifts, etc.

The principal challenges to theory are an improved description of continuum states, many body effects and open shells, relativistic effects and nuclear motion (both vibronic coupling and dissociation). This is by no means trivial as it requires the inclusion of additional degrees of freedom, both electronic and vibrational, and their coupling, enormously increasing the dimensionality of the problem. One has to learn to devise effective models to make problems tractable.

On the experimental side, precise data over a larger energy range and angular distribution information will provide the data required. This requires improved resolution and better statistics, necessitating improvement in instrumentation and the facility for handling delicate samples over long acquisition times, a scarce resource at present SR facilities. Pulsed field ionization photoelectron spectroscopy (PFI–PES), which has been recently implemented using synchrotron sources, provides extremely high resolution spectra [67], yet the challenge of studying stable transition metal complexes has yet to be met.

The close link between gas phase studies of isolated molecules and transition metal systems in the solid state must be stressed. These are of paramount technological importance and include bulk materials, surfaces and adsorbates, which can be understood and modelled by finite clusters, due to the localized nature of the excitation process.

Thorough treatment of key classes of inorganic compounds by this dual approach enables more confident deductions for systems where experimental data are accessible but which are difficult to treat computationally at a high level.

Acknowledgements

Both of us wish to acknowledge and thank our scientific collaborators who have engaged with us in this research.

References

[1] D.W. Turner, C. Baker, A.D. Baker, C.R. Brundle, Molecular Photoelectron Spectroscopy, Wiley, London, 1970.
[2] A. Cowley, Prog. Inorg. Chem. 26 (1979) 46.
[3] J.C. Green, Struct. Bond. 43 (1981) 37.
[4] J.C. Green, in: R.B. King (Ed.), Encyclopedia of Inorganic Chemistry, vol. 6, Wiley, Chichester, 1994, p. 3257.
[5] J.C. Green, Acc. Chem. Res. 27 (1994) 131.
[6] G.M. Bancroft, Y.F. Hu, in: E.I. Solomon, A.B.P. Lever (Eds.), Inorganic Electronic Structure and Spectroscopy, vol. 1, Wiley, New York, 1999, p. 443.
[7] U. Gelius, K. Siegbahn, Faraday Discuss. Chem. Soc. 54 (1972) 257.
[8] U. Gelius, Electron Spectroscopy, North-Holland, Amsterdam, 1972.
[9] E.I. Solomon, L. Basumallick, P. Chen, P. Kennepohl, Coord. Chem. Rev. 249 (2005) 229.
[10] V. Schmidt, Phys. Lett. A 45 (1973) 63.
[11] P.K. Ghosh, Introduction to Photoelectron Spectroscopy, Wiley, New York, 1983.
[12] S.T. Manson, D. Dill (Eds.), The photoionization of atoms, Cross-Sections and Photoelectron Angular Distributions, vol. 2, Academic Press, New York, 1978, p. 157.
[13] G. Cooper, J.C. Green, M.P. Payne, B.R. Dobson, I.H. Hillier, J. Am. Chem. Soc. 109 (1987) 3836.
[14] C.N. Field, J.C. Green, N. Kaltsoyannis, G.S. McGrady, A.N. Moody, M. Siggel, M. DeSimone, J. Chem. Soc., Dalton Trans. 1997, p. 213.
[15] J.J. Yeh, I. Lindau, At. Data Nucl. Data Tables 32 (1985) 1.
[16] J.W. Cooper, Phys. Rev. 128 (1962) 681.
[17] J.W. Cooper, Phys. Rev. Lett. 13 (1964) 762.
[18] R.D. Cowan, The Theory of Atomic Structure and Spectra, Chemical Abstracts Service, Columbus, Ohio, 1981.
[19] S.T. Manson, J.W. Cooper, Phys. Rev. 165 (1968) 126.
[20] U. Fano, Phys. Rev. 124 (1961) 1866.
[21] U. Fano, J.W. Cooper, Phys. Rev. A 137 (1965) 1364.
[22] J.G. Brennan, J.C. Green, C.M. Redfern, J. Am. Chem. Soc. 111 (1989) 2373.
[23] G. Cooper, J.C. Green, M.P. Payne, Mol. Phys. 63 (1988) 1031.
[24] M. Stener, P. Decleva, A. Lisini, J. Phys. B: At. Mol. Opt. Phys. 28 (1995) 4973.
[25] J.L. Dehmer, J. Chem. Phys. 56 (1972) 4496.
[26] J.L. Dehmer, in: D.G. Truhlar (Ed.), Resonances in Electron–Molecule Scattering, van der Waals Complexes, and Reactive Chemical Dynamics, vol. 263, American Chemical Society, Washington, DC, 1984.
[27] P.W. Langhoff, in: D.G. Truhlar (Ed.), Resonances in Electron–Molecule Scattering, van der Waals Complexes and Reactive Chemical Dynamics, vol. 263, American Chemical Society, Washington, DC, 1984.
[28] J.L. Dehmer, A.C. Parr, S.H. Southworth, in: G.W. Marr (Ed.), Handbook of Synchrotron Radiation, vol. 2, North-Holland, Amsterdam, 1987, p. 241.
[29] J. Tse, J. Chem. Phys. 89 (1988) 920.
[30] J.D. Bozek, G.M. Bancroft, J.N. Cutler, K.H. Tan, B.W. Yates, J.S. Tse, Chem. Phys. 132 (1989) 257.
[31] B.E. Bursten, J.C. Green, N. Kaltsoyannis, M.A. MacDonald, K.H. Sze, J.S. Tse, Inorg. Chem. 33 (1994) 5086.
[32] J.C. Green, M.F. Guest, I.H. Hillier, S.A. Jarrett-Sprague, N. Kaltsoyannis, M.A. MacDonald, K.H. Sze, Inorg. Chem. 31 (1992) 1588.
[33] J. Brennan, G. Cooper, J.C. Green, M.P. Payne, C.M. Redfern, J. Electr. Spectrosc. Rel. Phenom. 66 (1993) 101.
[34] J.C. Green, N. Kaltsoyannis, K.H. Sze, M. MacDonald, J. Am. Chem. Soc. 116 (1994) 1994.
[35] J.G. Brennan, G. Cooper, J.C. Green, N. Kaltsoyannis, M.P. Payne, C.M. Redfern, K.H. Sze, M.A. MacDonald, Chem. Phys. 164 (1992) 271.
[36] J.B. West, P.R. Woodruff, K. Codling, R.G. Houlgate, J. Phys. B. 9 (1976) 407.
[37] N. Kaltsoyannis, J. Chem. Soc., Dalton Trans. (1995) 3727.
[38] S. Evans, M.F. Guest, I.H. Hillier, A.F. Orchard, J. Chem. Soc., Faraday Trans. 2 (1974) 417.
[39] C.N. Field, J.C. Green, M. Mayer, V.A. Nasluzov, N. Rosch, M.R.F. Siggel, Inorg. Chem. 35 (1996) 2504.
[40] X. Li, J.S. Tse, G.M. Bancroft, R.J. Puddephatt, K.H. Tan, Inorg. Chem. 35 (1996) 2515.
[41] A. Lisini, P.I.J.Q.C. Decleva, Int. J. Quantum Chem. 55 (1995) 281.
[42] B.O. Roos, K. Andersson, M.P. Fülscher, P.Å. Malmqvist, L. Serrano-Andrés, K. Pierloot, M. Merchàn, Adv. Chem. Phys. 93 (1996) 219.
[43] W. Von Niessen, J. Schirmer, L.S.C.P.R. Cederbaum, Comput. Phys. Rev. 1 (1984) 57.
[44] M.M. Rohmer, J. Demuyinck, A. Veillard, Theor. Chim. Acta 36 (1974) 93.
[45] X. Li, G.M. Bancroft, R.J. Puddephatt, Z.F. Liu, Y.F. Hu, K.H. Tan, J. Am. Chem. Soc. 116 (1994) 9543.
[46] P. Decleva, G. Fronzoni, A. Lisini, in: J.K. Labanowski, J.W. Andzelm (Eds.), Density Functional Methods in Chemistry, Springer, New York, 1991, p. 323.
[47] C. Burney, Part II, Oxford University, 2001.
[48] E.J. Baerends, 2002.2 ed., Scientific Computing and Modelling NV Vrije Universiteit, Amsterdam, 2002.
[49] M. Ohno, W. von Niessen, J. Schüle, Chem. Phys. 158 (1991) 1.
[50] B.E. Bursten, J.C. Green, N. Kaltsoyannis, Inorg. Chem. 33 (1994) 2315.
[51] J. Brennan, G. Cooper, J.C. Green, M.P. Payne, C.M. Redfern, J. Electron Spectrosc. Relat. Phenom. 73 (1995) 157.
[52] M. Stener, G. Fronzoni, D. Toffoli, P. Decleva, Chem. Phys. 282 (2002) 337.
[53] G. Fronzoni, G.M. Stener, P. Decleva, J. Chem. Phys. 118 (2003) 10051.
[54] M. Stener, P. Decleva, J. Chem. Phys. 112 (2000) 10871.
[55] M. Stener, P. Decleva, I. Cacelli, R. Moccia, R. Montuoro, Chem. Phys. 272 (2001) 15.
[56] M. Stener, S. Furlan, P. Decleva, Phys. Chem. Chem. Phys. 3 (2001) 19.
[57] M. Venuti, M. Stener, P. Decleva, Chem. Phys. 234 (1998) 95.
[58] H. Bachau, E. Cormier, P. Decleva, J.E. Hansen, F. Martin, Rep. Prog. Phys. 64 (2001) 1815.
[59] E.J. Baerends, D.E. Ellis, P. Ros, Chem. Phys. 2 (1973) 41.
[60] R. Van Leeuwen, E. Baerends, J. Phys. Rev. A 49 (1994) 2421.
[61] G. Fronzoni, P. Colavita, M. Stener, G. De Alti, P. Decleva, J. Phys. Chem. A 105 (2001) 9800.

[62] M.N. Piancastelli, P.R. Keller, J.W. Taylor, F.A. Grimm, T.A. Carlson, J. Am. Chem. Soc. 105 (1983) 4235.
[63] M. Stener, G. Fronzoni, S. Furlan, P. Decleva, J. Chem. Phys. 114 (2001) 306.
[64] G. Fronzoni, M. Stener, S. Furlan, P. Decleva, Chem. Phys. 273 (2001) 117.
[65] M.R. Hermann, P.W. Langhoff, Chem. Phys. Lett. 82 (1981) 242.
[66] J.K. Padden Metzker, N.E. Gruhn, D.L. Lichtenberger, J. Phys. Chem. A 106 (2002) 9999.
[67] C.-K. Ng, Annu. Rev. Phys. Chem. 53 (2002) 101.
[68] Y.F. Hu, G.M. Bancroft, Z.F. Liu, K.H. Tan, Inorg. Chem. 34 (1995) 3716.
[69] H.B. Davis, R.K. Pomeroy, Y.F. Hu, G.M. Bancroft, K.H. Tan, Chem. Phy. Lett. 252 (1996) 267.
[70] X.R. Li, G.M. Bancroft, R.J. Puddephatt, Y.F. Hu, Z. Liu, D.G.J. Sutherland, K.H. Tan, J. Chem. Soc., Chem. Comm. (1993) 67.
[71] X. Li, J.S. Tse, G.M. Bancroft, R.J. Puddephatt, K.H. Tan, Organometallics 14 (1995) 4513.
[72] C.N. Field, J.C. Green, A.G.J. Moody, M.R.F. Siggel, Chem. Phys. 206 (1996) 211.
[73] Y.F. Hu, G.M. Bancroft, K.H. Tan, Inorg. Chem. 39 (2000) 1255.
[74] X.R. Li, G.M. Bancroft, R. Puddephatt, J. Accounts Chem. Res. 30 (1997) 213.
[75] X. Li, G.M. Bancroft, R.J. Puddephatt, Y.-F. Hu, K.H. Tan, Organometallics 15 (1996) 2890.
[76] D.S. Yang, G.M. Bancroft, R.J. Puddephatt, K.H. Tan, J.N. Cutler, J.D. Bozek, Inorg. Chem. 29 (1990) 4956.
[77] M. de Simone, M. Coreno, J.C. Green, S. McGrady, H. Pritchard, Inorg. Chem. 42 (2003) 1908.
[78] J.G. Brennan, J.C. Green, C.M. Redfern, M.A. MacDonald, J. Chem. Soc., Dalton (1990) 1907.
[79] C.E. Davies, J.C. Green, N. Kaltsoyannis, M.A. MacDonald, J. Qin, T.B. Rauchfuss, C.M. Redfern, G.H. Stringer, M.G. Woolhouse, Inorg. Chem. 31 (1991) 3779.
[80] X. Li, G.M. Bancroft, R.J. Puddephatt, Z. Yuan, K.H. Tan, Inorg. Chem. 35 (1996) 5040.